Published in Journal of Geophysical Research 110 : B06402, 2005
which should be used for any reference to this work

Irregular earthquake cycle along the southern Tianshan front, Aksu area, China

Aurélia Hubert-Ferrari,[1,2] John Suppe,[2] Jerome Van Der Woerd,[3] Xin Wang,[4] and Huafu Lu[5]

Received 28 May 2003; revised 10 January 2005; accepted 1 February 2005; published 11 June 2005.

[1] A long deformation record (~16.5 ka) showing nonsteady earthquake recurrence is established for the Aksu thrust (Tianshan, China) on the basis of cosmogenic ^{10}Be dating of faulted surfaces. Topographic leveling across the Aksu fault scarp indicates up to ~10 m uplift across a moraine abandoned ~16.5 ka and similar uplift of ~6 m across two inset surfaces yielding ages of ~12.5 and ~5 ka. Successively smaller uplifts of terraces younger than 5 ka indicate that three or more major earthquakes occurred during this period. These data show that the Aksu thrust fault was quiet for at least 7500 years and active in the last ~5000 years and probably in the interval 16.5–12.5 ka. The seismic cycle along the Aksu thrust fault over the last ~16,500 years was thus strongly irregular showing long quiescence and clustering, which is a challenge for paleoseismology and hazard assessment. This irregularity also makes it more difficult to estimate long-term shortening rates. Nevertheless, we are able to constrain a minimum total shortening rate (>7 mm/yr) across the southern Tianshan front for the last 12,500 years that is about a third of the total geodetic rate for the western Tianshan (~20 mm/yr).

1. Introduction

[2] Faults grow essentially by repeated earthquakes, but how this repetition occurs until recently has been a matter of debate. The most common hypothesis is that earthquakes with similar magnitude and characteristic slip occur regularly. This model is called the characteristic earthquake model. It is a direct consequence of the idea that constant and continuous loading at depth of a given fault is released regularly by repeated characteristic earthquakes. This earthquake model is heavily used in hazard assessments to estimate recurrence interval and maximum intensity damage.

[3] Historical earthquake records [*Ambraseys*, 1989; *Vere-Jones and Ozaki*, 1982; *Xu and Deng*, 1996; *Goes*, 1996] and paleoseismologic data [*Jacoby et al.*, 1998; *Grant and Sieh*, 1995; *Marco et al.*, 1996; *Wells et al.*, 1999] have, however, shown that earthquake recurrence time and earthquake-related slip on a given fault can show great variations. These variations are yet poorly understood though several models predict irregular behavior [*Bak and Tang*, 1989; *Carlson and Langer*, 1989; *Ben-Zion*, 1996; *Shaw and Rice*, 2000]. Therefore to reach a deeper understanding of seismic behavior of individual faults we need to have a well-constrained record of their long-term behavior, which is commonly difficult to obtain. However, in exceptional circumstances long-term records can be obtained through modern techniques of geomorphology, which is the focus of this paper.

[4] Constraining the long-term deformation of faults is feasible only if datable markers like alluvial deposits have clearly recorded fault growth over the appropriate timescale. At the front of the Tianshan Mountains, the major Aksu thrust fault uplifts a number of geomorphic surfaces, which can be used to constrain its seismic history over the last 16,500 yrs. To retrieve this long-term deformation record, we apply two different techniques. First, topographic leveling on each uplifted surface defines the shape of the cumulative fault scarps and the total deformation of each surface. Second, ^{10}Be cosmogenic dating determines the ages of the uplifted surfaces. By combining dating and leveling data we obtain a time-integrated slip history of the Aksu thrust fault.

2. Regional Framework

[5] The Tianshan is an active intracontinental mountain belt [*Molnar and Tapponnier*, 1975; *Tapponnier and Molnar*, 1979] that accommodates an important part of the present shortening between India and Asia, up to 40% in the western Tianshan [*Abdrakhmatov et al.*, 1996; *Reigber et al.*, 2001] (Figure 1a). The Tianshan extends laterally over ~2000 km with active thrusting occurring on both sides

[1]Institut de Géologie, Université de Neuchatel, Neuchâtel, Switzerland.
[2]Department of Geosciences, Princeton University, Princeton, New Jersey, USA.
[3]Institut de Physique du Globe de Strasbourg, CNRS UMR 7516, Strasbourg, France.
[4]Geosciences Department, Zhejiang University, Hangzhou, China.
[5]Department of Earth Sciences, Nanjing University, Nanjing, China.

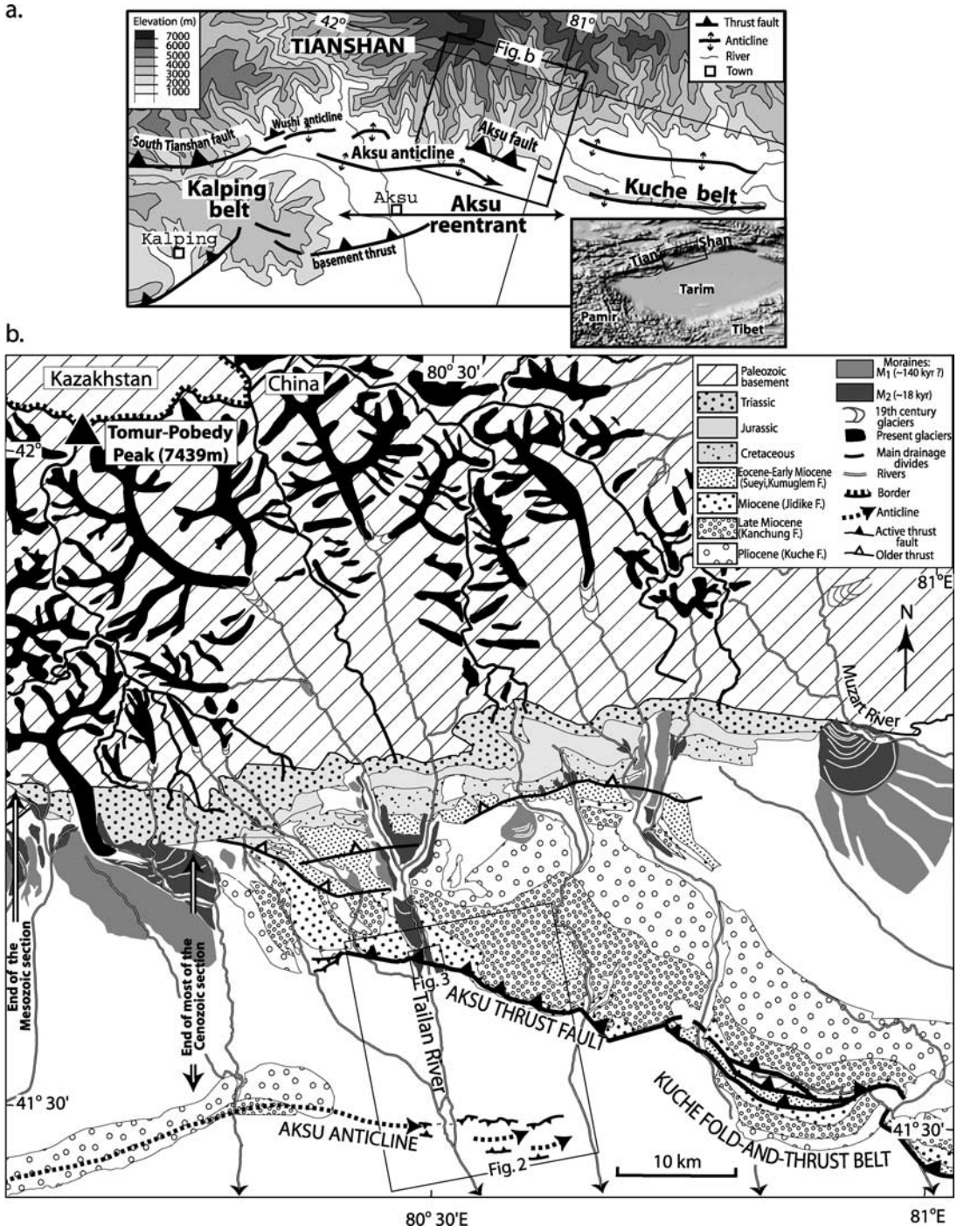

Figure 1. (a) Location of Tianshan range within the framework of the Indo-Eurasia collision. Deformation along southern Tianshan makes a reentrant near Aksu. Box is area of Figure 1b. (b) Morphotectonic map of eastern part of Aksu reentrant, where the thick Mesozoic-Cenozoic section deformed in the Kuche fold-and-thrust belt terminates toward west. Mountainsides are covered with glaciers and older glacial deposits that outcrop in front of present active glaciers. Two main active structures accommodate deformation: the Aksu thrust fault, which is the object of this study, and the Aksu anticline. Boxes are areas of Figures 2 and 3.

and within the belt [*Avouac et al.*, 1993; *Burbank et al.*, 1999; *Burchfiel et al.*, 1999; *Thompson et al.*, 2002]. Along the central southern Tianshan, deformation has propagated into the Tarim basin except in the Aksu reentrant (Figure 1a), where a drastic change in stratigraphy occurs. East of Aksu, folding in the Kuche belt involves a 7–8 km thick Mesozoic and Cenozoic section of continental sediments [*Yin et al.*, 1998; *Burchfiel et al.*, 1999] (Figure 1b). Mesozoic and most Cenozoic strata are absent west of Aksu where emergent imbricates of the

Kalping belt involve a 3.5 km thick largely cratonic upper Cambrian-Devonian section overlain by a Carboniferous to Permian foredeep section [*Allen et al.*, 1999]. In the Aksu reentrant between the Kuche and the Kalping belts (~80°30′E, Figure 1b), deformation lies right at the front of the high Tianshan range, and two active structures, the Aksu thrust fault and the Aksu anticline, deform Quaternary sediments.

[6] The Aksu thrust fault lies at the western end of the Kuche belt and bounds the southern flank of the high Tianshan massif where it reaches its highest elevation at Pobedy Peak (7439 m, Figure 1b). The Tianshan range in this area is the site of a number of active glaciers that extended as far south as the active mountain front during the last ice age, as shown by abandoned moraines (Figure 1b) [*Zheng*, 1986; *Zhang and Shao*, 1991]. Surface geology and seismic reflection profiles put some constraints on the Aksu thrust fault geometry. The fault plane has a shallow north dip of ~20° constrained by field measurements in several river valleys. A similarly shallow dip was seen in unpublished seismic reflection profiles that cross the fault ~10–20 km to the east. The fault appears to flatten to a detachment about 8 km to the north in the area where Pliocene strata covered by young alluvial/moraine deposits are present (Figure 1b). The Aksu thrust fault involves only Cenozoic strata and runs along a detachment near the base of the evaporite-rich continental Kanchung Formation (Figure 1b). The fault terminates to the west where this Cenozoic section disappears.

3. Geomorphic Characteristics of Uplifted Surfaces in the Tailan Valley

[7] The Aksu thrust fault cuts and uplifts a variety of surfaces along the Tailan river valley (Figures 2 and 3): morainic deposits, alluvial terraces and a major debris avalanche. The remnants of a terminal moraine outcrop on the flanks of the river valley and the other geomorphic surfaces are nested inside closer to the present river course (Figure 3). We labeled these surfaces from the highest to the lowest: M, T_0, $T_{0\text{-}1}$, $T_{0\text{-}2}$, $T_{0\text{-}3}$, and $T_{0\text{-}4}$.

[8] The moraine (M) is located about 50 to 70 m above the present river channel. Its surface shows a very rough topography with troughs and ridges of several meters, inherited from successive minor glacial retreats and/or advances. The morainic surface is also paved with blocks of very different types and sizes, some larger than several meters.

[9] The T_0 surface is a main outwash terrace located on the western side of the present river 17 m below the moraine. The T_0 surface is paved with very diverse boulders, cobbles and pebbles that are most probably reworked morainic elements (Figure 4a). However, the mean size of the alluvium deposited is an order of magnitude smaller than the size of morainic material. Several gullies and rills incise the T_0 surface.

[10] The $T_{0\text{-}1}$ surface is a large-scale debris avalanche deposit, with blocks as large as 5–10 m rising above its general surface, that covers the piedmont south of the Aksu thrust over an area of at least 40 km^2 (see Appendix A for a complete description; Figure 2). Near the mountain front, $T_{0\text{-}1}$ crops out extensively on the eastern side of the present riverbed between the moraine and the T_0 terrace at an elevation 15 m below T_0 (Figure 3). On the west side of the Tailan River there is a local terrace fragment, adjacent to the T_0 terrace riser and cut by the fault, which is likely the $T_{0\text{-}1}$ surface, given its elevation. The $T_{0\text{-}1}$ surface is a smoother surface than T_0, paved with smaller, more rounded pebbles and cobbles (Figure 4). The $T_{0\text{-}1}$ surface is much less incised by rills than T_0.

[11] The $T_{0\text{-}2}$, $T_{0\text{-}3}$, and $T_{0\text{-}4}$ surfaces are three minor alluvial terraces located on the eastern side of the Tailan River and below $T_{0\text{-}1}$ (Figures 3 and 4b). These terraces extend only locally a few hundred meters across the fault zone. Terrace $T_{0\text{-}2}$ is located west of and 5 m below $T_{0\text{-}1}$. Terrace $T_{0\text{-}3}$ is closer to the present active channel to the west and is discontinuous across the fault. $T_{0\text{-}3}$ is 4 m below $T_{0\text{-}2}$ and 2 m above $T_{0\text{-}4}$. Finally, terrace $T_{0\text{-}4}$ lies 10 m above the present riverbed.

[12] The characteristics, locations and respective heights of the different geomorphic surfaces suggest the following emplacement history in the Tailan river valley. During the last glacial period (~20–16 ka) a glacier probably filled the entire 2.7-km-wide Tailan valley at the mountain front (Figure 2). Later during the Holocene, while the glacier melted to reach its present position about 30 km upstream, the Tailan River incised and removed the terminal morainic material over a width of ~1.2 km (Figure 3). Several alluvial terraces and a debris avalanche were subsequently deposited inside this new river valley. The sequence of heights of the different postmoraine geomorphic surfaces determines their age sequence. The highest T_0 surface was thus emplaced first, probably shortly after the retreat of the glacier during the last glacial/interglacial climatic transition. The debris avalanche $T_{0\text{-}1}$ and the minor alluvial terraces $T_{0\text{-}2}$, $T_{0\text{-}3}$, and $T_{0\text{-}4}$ were deposited subsequently during the Holocene.

4. Characteristics of the Aksu Thrust Scarp in the Tailan Valley

4.1. Measurements

[13] Topographic leveling across the Aksu thrust fault scarp constrains the uplift and tilt of each surface and the fault scarp shape. Topographic profiles were measured using a reflectorless laser. The intrinsic precision of the instrument and the length of the profiles (<500 m) ensure that the instrumental errors are at most a few decimeters over each profile and <5 cm for the scarp profiles, which were surveyed at close range. Consequently, the intrinsic roughness of the surface is the main source of error. Nineteen topographic profiles leveled in the field (see location on Figure 5) were projected on a vertical plane perpendicular to the local fault strike (Figure 6).

[14] Measuring scarp height is not straightforward because most regional surface slopes north and south of the scarp are different. To be able to get reliable and equivalent scarp height measurements, we applied the following method. For each surface, we used the longest profile available and obtained regional slopes north and south of the scarp by fitting data points to a straight line. We then determined if the surface slopes obtained agreed with profiles on the same surface, especially for surface T_0 for which we surveyed a number of profiles. Finally

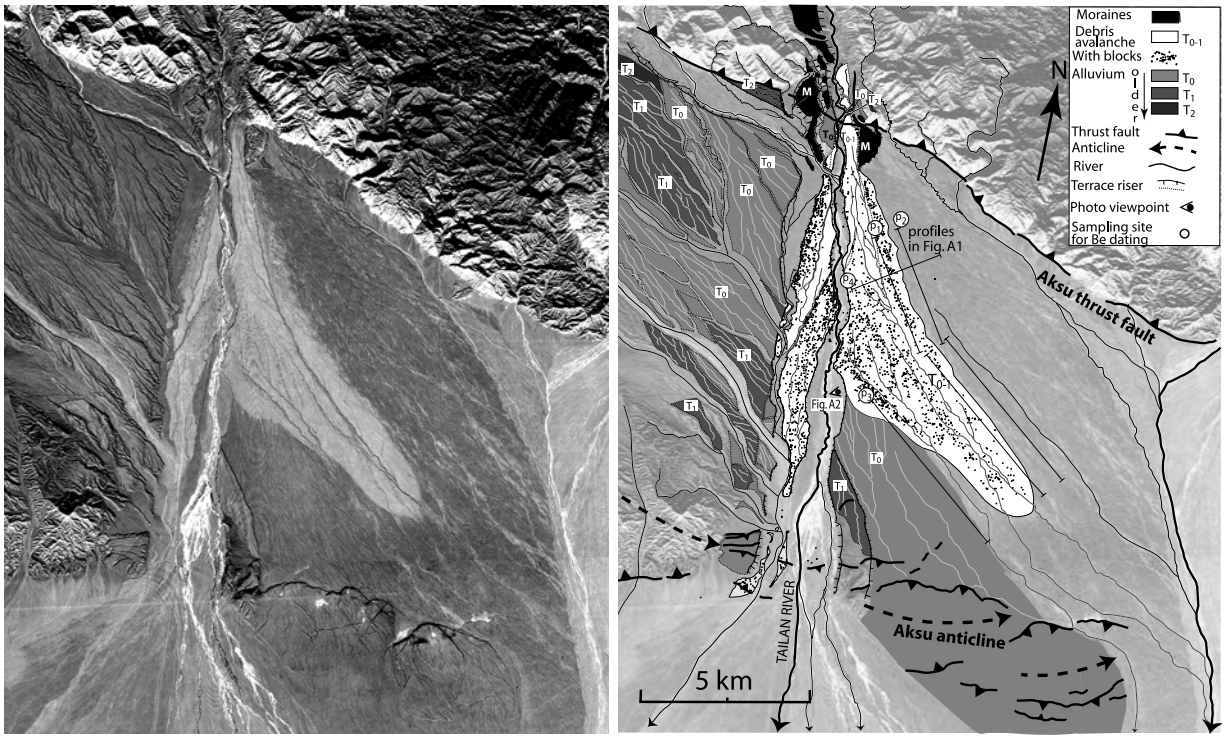

Figure 2. Tailan river valley (see location in Figure 1b): (left) Corona image of the area and (right) morphological interpretation. To the south the Aksu anticline deforms Quaternary alluvial surfaces labeled T_0 and T_1. To the north, along the mountain front, the Aksu thrust cuts across moraines (labeled M) that outcrop on both sides of Tailan valley and younger deposits. A huge debris avalanche, which splits into two lobes, was deposited between these two active structures. Debris avalanche surface is covered with scattered megablocks (Figure 9) and agglomerates outlined by small dots. Locations of Figures A1 and A2 are indicated.

the scarp height was obtained by measuring the height between regional surfaces across the scarp at the inflexion point where the scarp profile meets the inferred northern surface slope (see inset in Figure 6a).

[15] Errors associated with scarp measurements are directly linked to errors in regional slope estimates. For the long scarp profiles used to infer slopes on each surface, we estimate slope errors to be ±0.3°. Slope errors associated with the moraine are higher because the surface roughness is more important (see Figure 6c). For other profiles, we must add errors done by stacking the surface slope inferred previously to the observed slopes north and south of the scarp. To translate slope errors into scarp height errors the most important factor is the total difference in slope across the scarp. For terraces $T_{0\text{-}2}$, $T_{0\text{-}3}$, $T_{0\text{-}4}$ the difference in slope across the scarp does not exceed 1.7°, and we estimate the scarp height errors to be less than 0.5 m. For terraces T_0, and $T_{0\text{-}1}$ the scarp height errors are slightly higher and for the moraine they can reach more than 1 m.

4.2. Main Scarp Characteristics

[16] On the eastern side of the river, profiles p_1-p_2, p_3 and p_4-p_5-p_6, leveled across surfaces $T_{0\text{-}1}$, $T_{0\text{-}2}$ and $T_{0\text{-}3}$-$T_{0\text{-}4}$ respectively (Figure 5), show that the thrust fault scarp is narrow and well defined (Figure 6a). The debris avalanche deposit ($T_{0\text{-}1}$), which may have buried a previously existing scarp along its path, is uplifted by ∼6.1 m (Figures 4b and 6a). A 4.2- to 4.4-m-high scarp crosses the inset $T_{0\text{-}2}$ terrace and the smaller discontinuous $T_{0\text{-}3}$ terrace. A ∼3.3-m-high scarp cuts the youngest $T_{0\text{-}4}$ terrace. On the western side of the river, profiles p_8-p_9-p_{10} leveled across the T_0 surface (Figure 5) show that the T_0 scarp near the river channel has a shape, a width (∼15 m) and a height (∼5.1–5.6 m) similar to the $T_{0\text{-}1}$ scarp (Figure 6a). The T_0 scarp height is 0.5 to 1 m lower than the $T_{0\text{-}1}$ scarp only at this location. Farther west, the T_0 scarp height is identical or slightly higher than the $T_{0\text{-}1}$ scarp (Figure 6b). These scarp height variations are most probably due to minor along-strike variation of uplift during earthquake rupture.

[17] The long profiles also show that the hanging wall above the fault scarp is tilted forward (Figures 6a, 6b, and 6c) over a zone ∼90- to 130-m-wide north of the scarp (Figure 5). Thus there is a differential surface tilt across the fault scarp (Figure 6). South of the scarp, surfaces $T_{0\text{-}4}$, $T_{0\text{-}3}$, $T_{0\text{-}2}$, $T_{0\text{-}1}$ have 1.1° to 1.2° southward dipping slopes similar to the river gradient, but north of the scarp the slopes are steeper, ranging from 2.8° for $T_{0\text{-}2}$ and $T_{0\text{-}3}$ to 3.9° for $T_{0\text{-}1}$ (Figure 6a). Similarly, south of the fault trace the slope of surface T_0 is about ∼1.9°, and north of the scarp, it reaches 4.4° (Figure 6b). The difference in surface slopes across the scarp is thus 1.7° for $T_{0\text{-}2}$ and $T_{0\text{-}3}$, and 2.5° to 2.7° for T_0 and $T_{0\text{-}1}$. The amount of tilting thus correlates directly with the heights of the scarp: for $T_{0\text{-}2}$ and $T_{0\text{-}3}$ the tectonic tilt is equal to 1.7° and the scarp height to ∼4.2 m, for T_0 and $T_{0\text{-}1}$, the tectonic tilt is equal ∼2.6° and

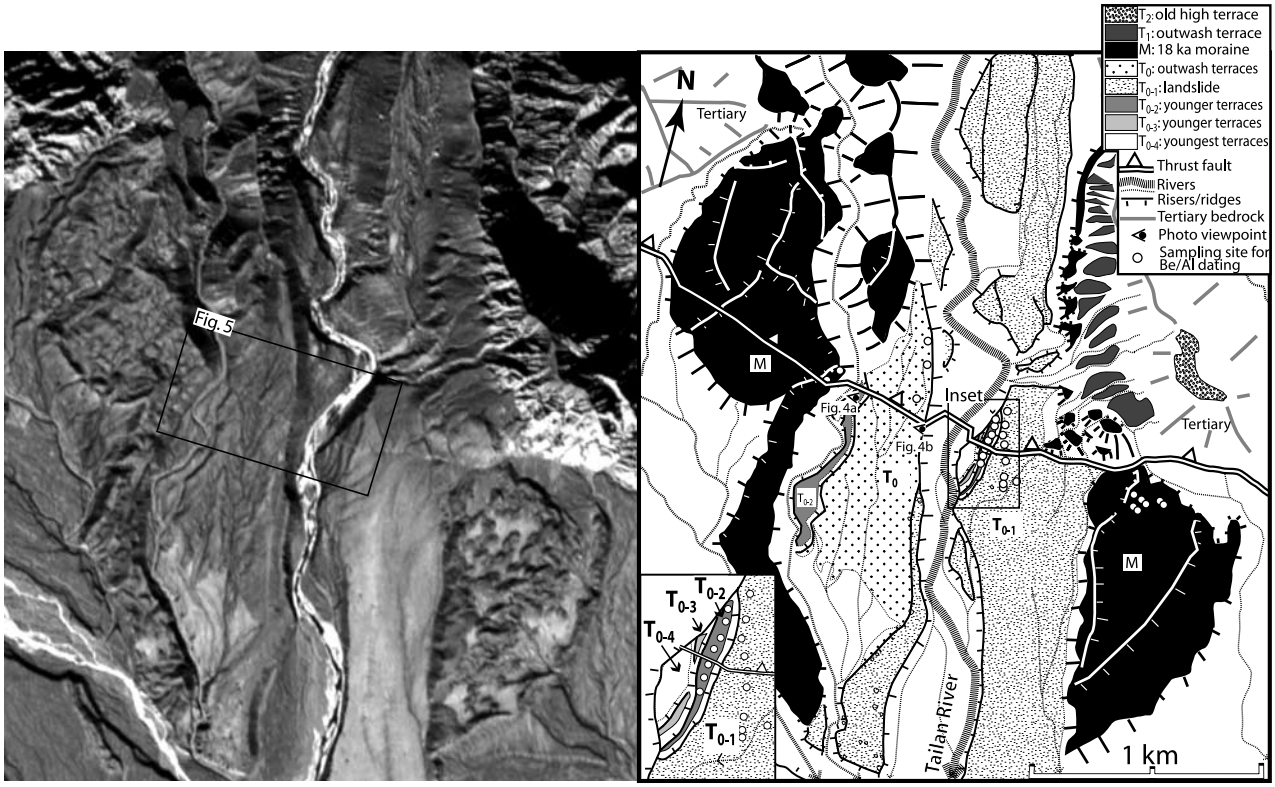

Figure 3. Morphological map of glacial and alluvial deposits vertically offset by the Aksu thrust fault along the Tailan river valley (see location on Figure 1b): (left) Corona image and (right) geomorphic interpretation. In the incised valley between remnant moraines (shown in black) are a number of younger nested surfaces, including a main outwash terrace (T_0), a debris avalanche surface (T_{0-1}), and additional minor alluvial terraces (T_{0-2}, T_{0-3} and T_{0-4}). The Aksu thrust fault cuts and uplifts all surfaces. White circles indicate relative positions of quartz-pebble samples on surfaces on either side of the fault. Inset is a blow up of the central part. Viewpoints of Figures 4a and 4b are shown.

the scarp height ~6 m. Thus along the Aksu thrust fault we have a fixed ratio of ~0.4° of tilt per meter of uplift.

4.3. Scarp Complexities Across Surface T_0 and the Moraine

[18] The simple scarp morphology across the lower surfaces near the Tailan river channel contrasts with the more complex scarp morphologies observed farther west across T_0 and across the moraine.

[19] Terrace T_0 shows a westward increase in scarp height (5.1–5.6 m along p_8-p_9-p_{10}, 6.2 m along p_{11}, 6.2–7.1 m along p_{12}, 6.3–7 m along p_{14}) and scarp width (compare profiles p_{11}, p_{12}, and p_{14}-p_{15} of Figure 6b). In addition, the scarp does not form a single step, but has a more complex shape characterized by several marked changes in slope. Along the T_0 western profiles, two main topographic steps are visible, labeled low and high subscarps in Figures 6b and 6c. Some of those subscarps display additional visible substeps of variable heights separated by distinctive flats. The most noticeable one is the low subscarp along p_{16} that is composed of three scarplets characterized by steep slopes with heights of 0.85 m, 1.5 m, 0.85 m, from south to north, respectively. This complex scarp morphology is probably related to the surface rupture process and may have diverse origins. Each scarplet might represent the surface rupture due to only one major earthquake that propagates farther south each time. Another possible explanation is that the rupture repeatedly splits near the surface in multiple closely spaced breaks.

[20] Across the moraine, the scarp morphology is more difficult to characterize because of the interplay between the complex scarp shape and the intrinsic large-scale roughness of the moraine surface. The moraine commonly has boulders with maximum diameters greater than 1 m and an intrinsic relief of moraine ridges similar to that of fault scarps. However, near the eastern riser of the moraine we can define unambiguously the moraine scarp by continuity with the nearby T_0 scarp (Figure 5). In this area, profiles p_{19} and p_{18} leveled across the moraine show two bumps over a width of 90 m corresponding to the T_0 low and high subscarps visible about 200 m to the east (Figure 6c). The cumulative scarp is 10.7 to 11.6 m high depending how we infer moraine slopes north and south of the scarp. In addition, the moraine does not show clear folding outside the 90-m-wide moraine scarp area. North and south of the scarp, the moraine has similar 1.2° to 1.9° slopes comparable to the slope of T_0 and T_{0-1} south of the scarp. The 10.7 to 11.6 m scarp height thus represents a direct measure of the total uplift of the moraine.

4.4. Total Uplift and Fault Scarp Model

[21] We cannot make a straightforward computation of the cumulated fault uplift across the different surfaces because of the ~90- to 130-m-wide zone of differential

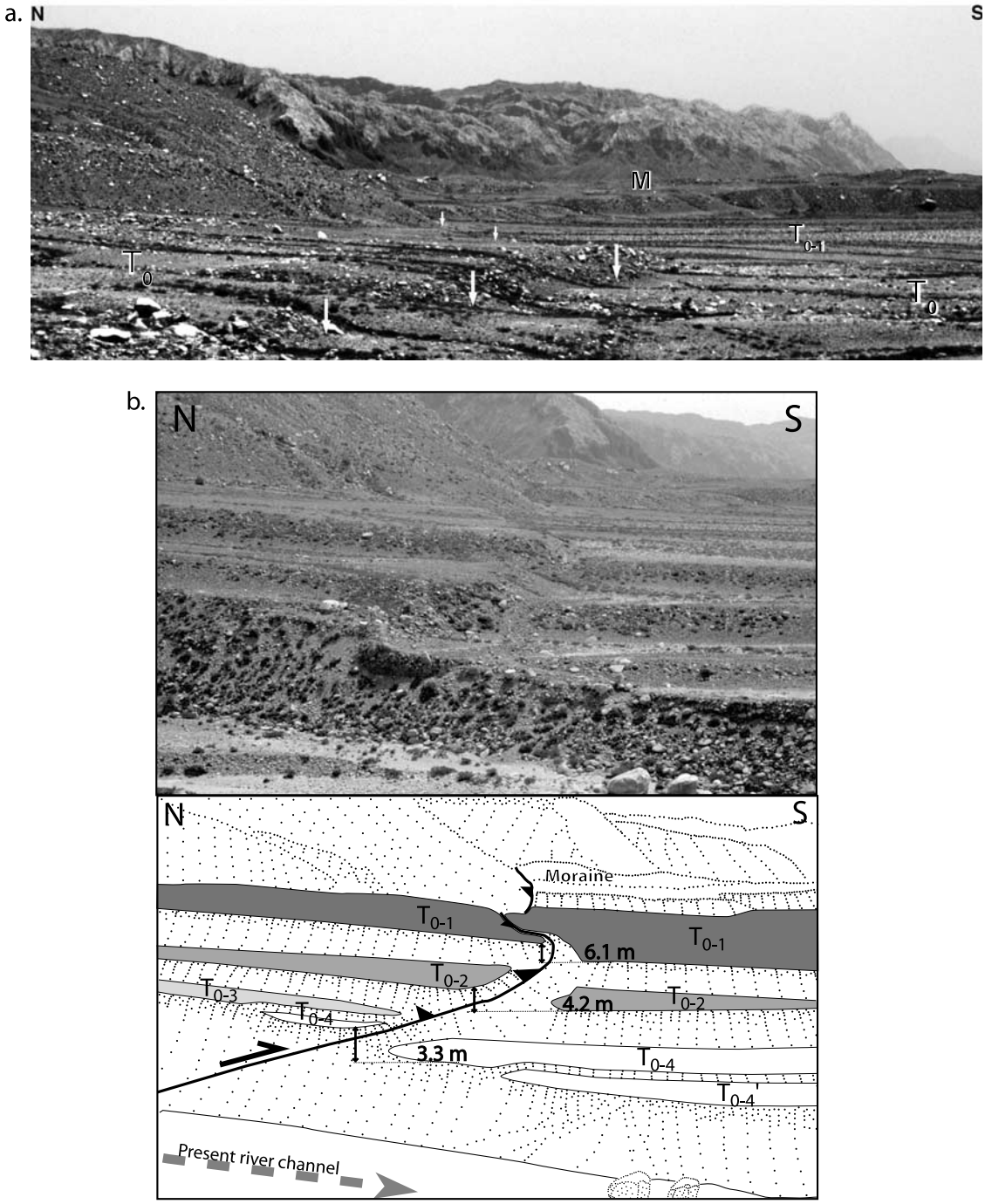

Figure 4. Photographs of surface offsets of the Aksu thrust (see viewpoint locations in Figure 3). (a) West of present river channel, fault scarp (white arrow) offsets across T_0 terrace, which has been incised by several gullies. (b) East of present river channel, thrust fault scarp, and vertical offsets across $T_{0\text{-}1}$, $T_{0\text{-}2}$, $T_{0\text{-}3}$ of 6.1 m, 4.2 m, and 3.3 m, respectively.

tilting occurring north of the scarp on most surfaces. For example, terrace T_0 is tilted differentially by 2.5° which contributes an additional ~9–11 m uplift for a total of 15–17 m uplift. As discussed before, the magnitude of the differential tilt for all profiles is correlated with scarp height (~0.4°/m). Therefore the tilting is clearly coupled to the faulting process, both occurring at the same time during earthquake rupture. The most straightforward mechanism to get a constant 0.4°/m partitioning between faulting and folding over a limited zone is to have an upward flattening of fault dip. Near-surface upward flattening of emergent thrusts is commonly seen in seismic lines, for example in

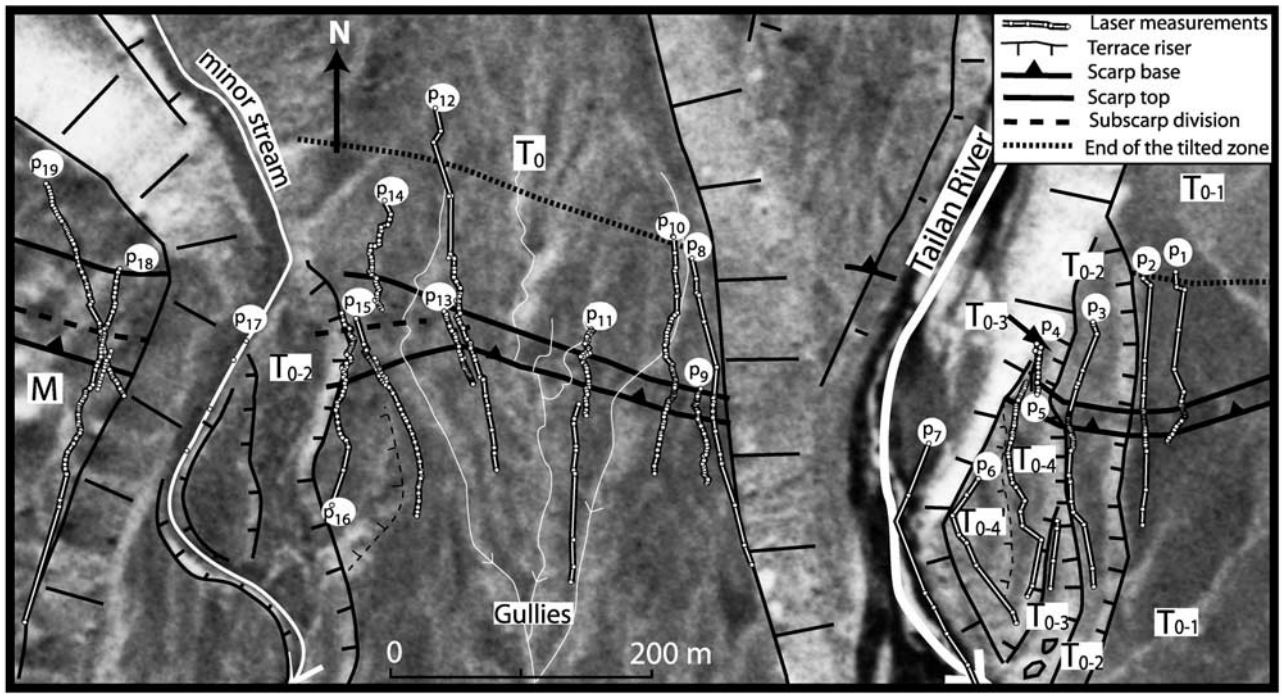

Figure 5. Locations of the 19 topographic profiles leveled across the Aksu thrust fault scarp (see location in Figure 3).

the Nankai Trough and Cascadia subduction zones [*Suppe et al.*, 2004] and is possibly dominated by compaction of the footwall [cf. *Xiao and Suppe*, 1989]. The Aksu thrust fault is not well exposed, but a downward steepening of the fault shape along the Tailan River is required by the locations of fault cuts on both sides of the river.

[22] To be able to get reliable slip amounts and thus shortening rates, we developed the following fault model. We used the fold shape of the T_0 surface near the Tailan River and the locations of the fault cuts on the $T_{0\text{-}1}$, $T_{0\text{-}2}$ and $T_{0\text{-}3}$ terraces with respect to the fault cut on T_0 as input data. Furthermore we know from bedrock outcrops in the nearby valleys and from seismic reflection profiles that the fault has a shallow $\sim 20^\circ$ mean dip. A series of kinematic models was then generated using the classic inclined shear method [*Gibbs*, 1983; *White et al.*, 1986]. We considered a wide range of possible dips for the folding vector ($50-90^\circ$), but there is a relatively narrow range of possible shallow fault shape models that would satisfy the data. The 2.5°observed tilt over a horizontal distance of 100 m on terrace T_0 and the locations of the fault cuts on other terraces could be fit only with a fault progressively flattening from a $\sim 22-23^\circ$ dip at depth to $\sim 11-14^\circ$ dip at the surface. Figure 7 shows the best fitting model of fault shape.

[23] The main output of the fault model is an input fault slip of $\sim$20 m for T_0 profile in Figure 7 which means $\sim$4 m of fault slip per meter of scarp height. Potential errors related to the fault model can reach a few meters. Note that whereas the folding of the T_0 surface is similar along strike, scarp height near the Tailan River is much lower than further west. So we estimate that fault slip recorded by T_0 is bracketed between 20 to 30 m.

[24] The flattening fault model developed to calculate slip rate applies only locally to alluvial surfaces near the Tailan River. The near-surface geometry of the Aksu thrust fault can vary along strike depending on the near-surface material it crosses. For example the moraine surface does not show any obvious north of the fault scarp, which implies that the dip of Aksu thrust fault across the moraine deposit is not changing. So for the moraine surface, we can compute directly the related fault slip using its total uplift (10.7–11.6 m) and a constant fault dip of 23°. The 27–30 m fault slip recorded by the moraine is to be compared to the 20–30 m minimum fault slip recorded by the T_0 terrace.

5. Ages of Surfaces Cut by the Aksu Thrust Fault

[25] Ages for the terraces and moraine were obtained from ^{10}Be-^{26}Al surface exposure dating [e.g., *Kohl and Nishiizumi*, 1992; *Bierman et al.*, 1995; *Gosse and Phillips*, 2001]. To account for possible different exposure histories, we performed multiple samplings on each surface [e.g., *Van der Woerd et al.*, 1998, 2002; *Lasserre et al.*, 2002; *Mériaux et al.*, 2004]. We sampled large embedded cobbles by breaking pieces from their top surfaces. We also collected smaller entire pebbles. A total of 32 samples for cosmogenic dating were collected on top of the highest moraine ridges and on surfaces T_0, $T_{0\text{-}1}$ and $T_{0\text{-}2}$ along paths perpendicular to the fault trace (Figure 3). More details concerning the sampling and the cosmogenic dating method can be found in the Appendix B.

[26] The ^{10}Be exposure ages obtained are listed in Table 1 and represented graphically in Figure 8. For each surface we computed an average age including all the samples. The moraine and T_0 ages, and the $T_{0\text{-}1}$ and $T_{0\text{-}2}$ ages have average values of $\sim 12-19$ ka and $\sim 4-5$ ka, respectively. These exposure ages are in agreement with the relative

height of the surfaces, their degree of weathering, and the height of the fault scarp uplifting them. Sample ages on the terraces tend to group into well-defined clusters whereas the moraine shows more scattered ages, as observed in other fluvioglacial settings [e.g., *Owen et al.*, 2003; *Mériaux et al.*, 2004]. To reduce age scattering, we defined outliers having a potential complex exposure history. Then we used the clustered sample ages excluding outliers to

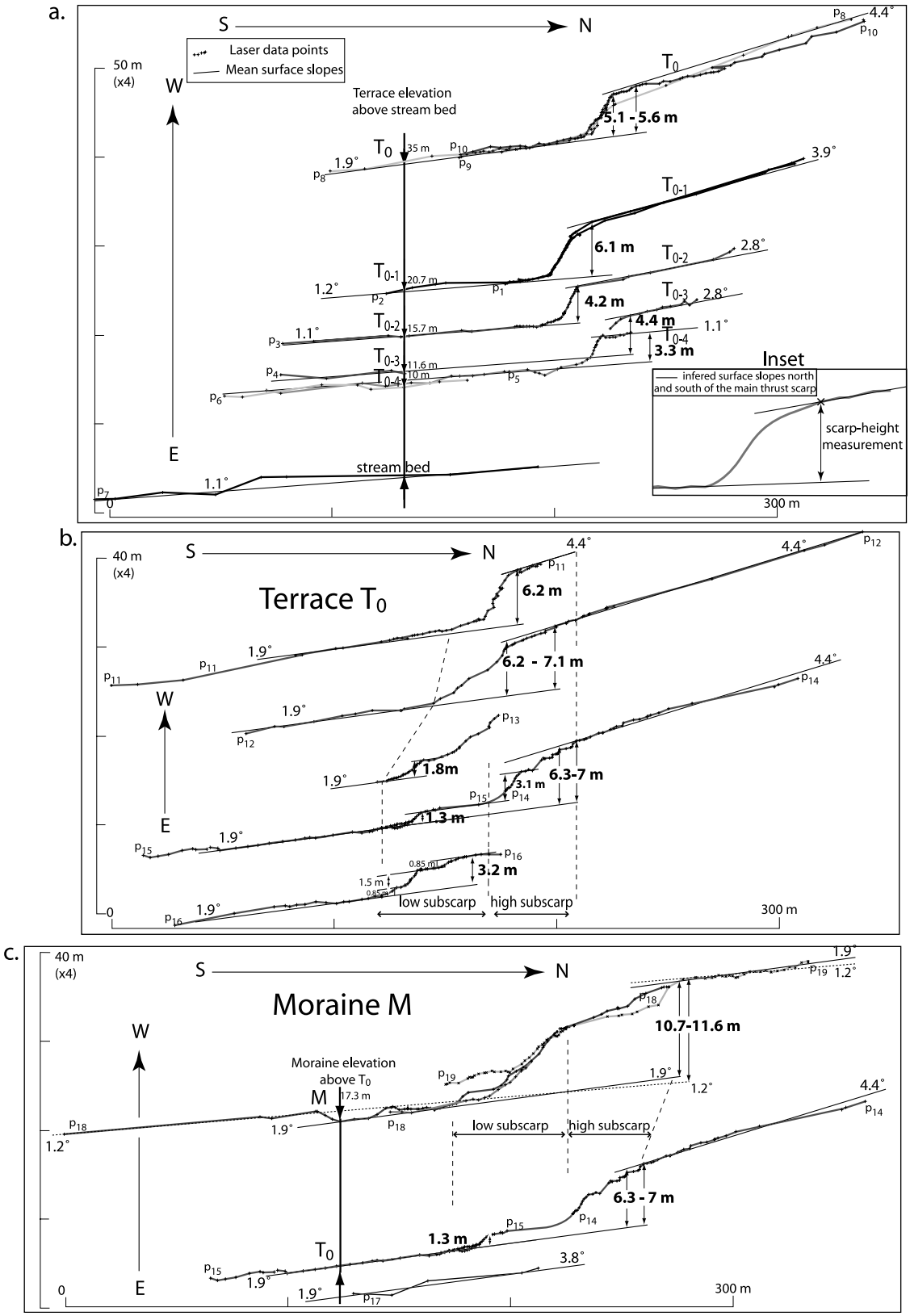

Figure 6

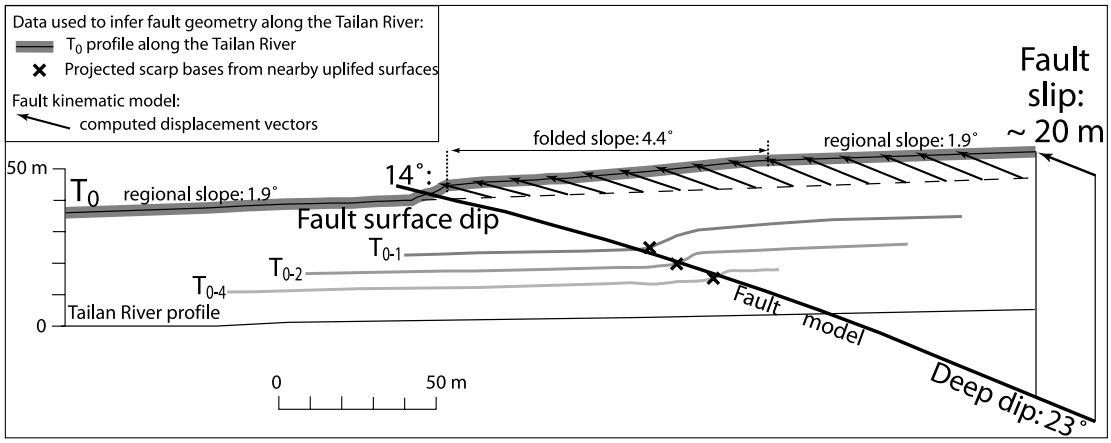

Figure 7. Fault model. Cross section along the Tailan River shows computed fault shape constrained by fold shape of T_0 surface and location of fault cuts on lower surfaces. The input fault dip of 22–23° is relatively robust for a range of folding vectors (90–50°N), computed using the inclined shear method [*Gibbs*, 1983; *White et al.*, 1986].

refine the surface ages [e.g., *Van der Woerd et al.*, 1998, 2002; *Mériaux et al.*, 2004].

[27] The age of terrace $T_{0\text{-}2}$ is tightly constrained with seven samples clustering at 4.1 ± 0.4 ka. On terrace $T_{0\text{-}1}$, from a total of 12 dated samples, four were samples taken on very large blocks or mounds scattered and embedded in the avalanche surface (Figure 9). The eight other samples cluster tightly around an average of 5.0 ± 0.3 ka with the exception of sample $T_{0\text{-}1}$-18_s (Figure 8). This markedly younger sample (3.5 ± 0.3 ka; Table 1) was sampled less than 10 m away from the fault scarp, where small rockfalls triggered by earthquakes may have rejuvenated part of the surface. All other anomalously young ages come from the large blocks embedded in the avalanche surface. Two samples ($T_{0\text{-}1}$-20_s: 3.9 ± 0.3 ka, and $T_{0\text{-}1}$-22_s: 4.2 ± 0.3 ka; Table 1) come from large granitic megaclasts strongly embayed and split by erosion. Local disintegration of these megaclasts may explain the younger ages. Two other samples ($T_{0\text{-}1}$-24_s and $T_{0\text{-}1}$-25_s) were collected 8 km to the south on the top of isolated 2-m-high mounds of large granitic clasts not covered with soil (locations on Figure 2) (Figure 9). They yield ages of 1.9 ± 0.2 ka and 3.1 ± 0.3 ka, 3 to 2 ka younger than the average age of $T_{0\text{-}1}$ (5 ± 0.3 ka; Table 1) (Figure 8). The young ages obtained may be related to the postdepositional evolution of these mounds characterized by removal of the soil/mud cover followed by rapid erosion with frequent rockfalls of their unconsolidated surface.

[28] The emplacement history of the debris avalanche $T_{0\text{-}1}$ and of the alluvial terrace $T_{0\text{-}2}$ can be refined on the basis of surface ages. The $T_{0\text{-}1}$ and $T_{0\text{-}2}$ ages cluster around close average values of 5.0 ± 0.3 ka and 4.1 ± 0.4 ka, respectively. The latter implies that terrace $T_{0\text{-}2}$ formed just after the emplacement of the $T_{0\text{-}1}$ avalanche and was abandoned soon afterward. This scenario is consistent with complex river adjustment after the avalanche. The debris of the avalanche blocked and filled the river valley with more than 10 m of sediments, thus strongly perturbing the river equilibrium. It is expected that after the avalanche the river would incise until it reached its former level possibly located just below the $T_{0\text{-}4}$ terrace. This process may have taken several thousand years, and the presence of terraces $T_{0\text{-}2}$, $T_{0\text{-}3}$, $T_{0\text{-}4}$ indicates that minor aggradational episodes occurred within this major incising trend.

[29] The three sample ages for the T_0 alluvial outwash surface (14.7 ± 1.9 ka) tend to overlap with the moraine ages. These data first suggest that the T_0 alluvium was emplaced rapidly after/during the retreat of the glacier, and that T_0 was incised forming an abandoned terrace shortly after its deposition. However, the number of dated samples is not enough to make a firm conclusion about the age and history of the T_0 surface. Another possibility would be that the two older samples of T_0 are reworked preexposed material from the moraine. Excluding these two samples would imply that T_0 has been emplaced around 12.5 ± 0.7 ka (Figure 9). This age is in fair agreement with ages of similar postglacial outwash terraces elsewhere, in the Tianshan [*Poisson and Avouac*, 2004], in north Tibet [*Van der Woerd et al.*, 2001, 2002; *Lasserre et al.*, 1999] and with the high level stands of lakes in northwestern Tibet [*Gasse et al.*, 1991; *Rhodes et al.*, 1996]. We thus infer that T_0 was emplaced between 12.5 and 14.5 ka, most probably around 12.5 ka.

Figure 6. Vertical cumulative uplift and height above active river bed of surfaces T_0, $T_{0\text{-}1}$, $T_{0\text{-}2}$, $T_{0\text{-}3}$, and $T_{0\text{-}4}$ (see location of profiles in Figure 5). (a) Surfaces $T_{0\text{-}4}$, $T_{0\text{-}3}$, $T_{0\text{-}2}$, $T_{0\text{-}1}$ and T_0 with scarp heights of 3.3 m, 4.4 m, 4.2 m, 6.1 m, and 5.1–5.6 m, respectively. Folding of hanging wall is shown by the difference in slope across the scarp, which extends 90–130 m north of the scarp. This differential tilting increases with scarp height (~0.4°/m, see text). (b) Scarp shape and heights across surface T_0. Regional surface slope is inferred from profile p_{15}. (c) Scarp shape and heights across moraine M. Westernmost T_0 profile (p_{15}) is indicated as reference. Note that the surface slope of the moraine is not very well constrained (two possible slopes 1.9° and 1.2° are shown).

Table 1. Cosmogenic Age of 32 Samples Along the Tailan River[a]

Sample	^{10}Be, 10^4 atoms/g	^{26}Al, 10^4 atoms/g	Latitude-Altitude Correction	Geomagnetic Corr	^{10}Be Model Age, ka
M-1	21.72 ± 0.77	140.94 ± 15.43	3.9149	1.0609	16.12 ± 1.05
M-2[b]	30.11 ± 1.25	158.93 ± 16.73	3.9149	1.0594	11.63 ± 0.71
M-3	27.74 ± 0.8	138.06 ± 15.71	3.9345	1.0610	14.8 ± 0.85
T_0-4_n	22.83 ± 0.72	116.06 ± 12.4	3.8180	1.0613	12.54 ± 0.74
T_0-5_n	29.92 ± 1.23		3.8180	1.0589	16.41 ± 1.06
T_0-6_n	27.41 ± 0.74	148 ± 15.55	3.8180	1.0605	15.05 ± 0.86
T_{0-2}-7_n	8.26 ± 0.36	46.61 ± 5.28	3.8152	1.1087	4.73 ± 0.32
T_{0-2}-8_n	7.21 ± 0.35	44.67 ± 5.08	3.8152	1.1160	4.16 ± 0.29
T_{0-2}-9_n	7.08 ± 0.39	42.05 ± 5.69	3.8152	1.1175	4.09 ± 0.31
T_{0-2}-10_n	7.25 ± 0.32	47.65 ± 6.59	3.8152	1.1156	4.18 ± 0.28
T_{0-2}-11_s	6.23 ± 0.4	49.37 ± 5.89	3.8043	1.1200	3.62 ± 0.3
T_{0-2}-12_s	6.5 ± 0.29	34.7 ± 4.05	3.8043	1.1221	3.78 ± 0.25
T_{0-2}-13_s	7.67 ± 0.37	42.18 ± 4.92	3.8043	1.1115	4.42 ± 0.31
T_{0-1}-14_n	8.73 ± 0.37	43.68 ± 4.91	3.8344	1.1057	4.97 ± 0.33
T_{0-1}-15_n	9.24 ± 0.32	49.46 ± 5.56	3.8344	1.1002	5.23 ± 0.32
T_{0-1}-16_n	8 ± 0.4	51.71 ± 6.37	3.8344	1.1102	4.57 ± 0.32
T_{0-1}-17_n	8.9 ± 0.42	68.66 ± 9.3	3.8344	1.1038	5.06 ± 0.35
T_{0-1}-18_s[b]	6.05 ± 0.37	41.09 ± 6.34	3.8180	1.1185	3.5 ± 0.28
T_{0-1}-19_s	8.47 ± 0.41	64.09 ± 7.84	3.8180	1.1077	4.85 ± 0.34
T_{0-1}-20_t	6.7 ± 0.43	35.64 ± 4.6	3.8180	1.1222	3.89 ± 0.32
T_{0-1}-21_s	9.43 ± 0.41		3.8180	1.0978	5.35 ± 0.36
T_{0-1}-22_t	7.22 ± 0.36	40.27 ± 4.91	3.8180	1.1160	4.16 ± 0.3
T_{0-1}-23_s	8.82 ± 0.43		3.8180	1.1042	5.03 ± 0.35
M-24_s	30.97 ± 0.79	181.27 ± 19.08	3.9149	1.0589	16.57 ± 0.93
M-25_s	31.78 ± 0.94	162.77 ± 17.1	3.9149	1.0582	17 ± 0.99
M-26_s	27.98 ± 0.76	168.47 ± 18.1	3.9149	1.0608	14.99 ± 0.85
M-27_s[b]	20.28 ± 0.7	132.74 ± 14.77	3.9149	1.0600	10.85 ± 0.66
M-28_s	36.19 ± 0.95	243.82 ± 27.21	3.9149	1.0558	19.32 ± 1.09
M-29_s[b]	16.95 ± 0.56	116.48 ± 13.18	3.9149	1.0598	9.06 ± 0.54
M-30_s	34.2 ± 0.92	211.12 ± 23.56	3.9149	1.0568	18.27 ± 1.04
T_{0-1}-31_t	3.19 ± 0.39	27.55 ± 3.88	3.4879	1.0714	1.93 ± 0.25
T_{0-1}-32_t	4.94 ± 0.49	33.39 ± 5.34	3.4879	1.1111	3.09 ± 0.35

[a]Samples from 01 to 30 increase with sample longitude and are located near the Aksu fault scarp. Samples 31 and 32 are located about 8 km south of the scarp. Subscripts n and s refer to samples taken north and south of the fault trace, respectively; subscript t refers to samples taken on top of very large blocks embedded in the avalanche surface.

[b]Outliers excluded from calculation of mean "clustered" exposure age of a given surface (see Figure 8 and Appendix A).

[30] The 10 sample ages of the moraine remnants on both sides of the Tailan River range from 9 to 19 ka with an average over all the samples of 14.9 ± 3.3 ka. This scattering may have the following origins. First, the terminal moraine surface age may be diachronic as suggested by the absence of a clear ridge. Second, the terminal moraine may result from the successive accumulation over a large period of materials with different exposure histories. Finally, the high roughness of the moraine may favor frequent rockfalls along the hill-tops where all the samples were collected. If we exclude the samples with ages younger than ~12.5 ka (M-01: 11.6 ± 0.7 ka on the western moraine; M-27: 10.8 ± 0.7 ka and M-29: 9.1 ± 0.5 ka on the eastern moraine; Table 1), we obtain a clustered mean exposure age of the moraine of 16.7 ± 1.6 ka. This result suggests that the moraine was definitely abandoned by14.5 ka, after the pulse of the last glacial maximum (~18 ka [e.g., *Thompson et al.*, 1997]). The glacial retreat in the Tailan valley would thus be synchronous with timing of glacial retreat elsewhere, in the Karakorum [*Richards et al.*, 2000; *Owen et al.*, 1999; *Chevalier et al.*, 2004], in eastern Tibet [*Schäfer et al.*, 2002; *Mériaux et al.*, 2004], and in the Bogdashan region to the northeast of the Tianshan [*Zheng*, 1988].

[31] In summary, terrace T_{0-2} and debris avalanche T_{0-1} have well-constrained ^{10}Be ages of 4.1 ± 0.4 ka and 5.0 ± 0.3 ka, respectively, each based on seven concordant samples. Terrace T_0, less well constrained by only three ages, may be as old as 14.5 ka, clearly postdating the last maximum advance of the Tailan glacier at ~16.5 ka.

6. Irregular Seismic Cycle Inferred Along the Aksu Thrust Fault

6.1. Assumptions

[32] We combine the ages and the scarp height profiles to get a time-integrated slip history of the Aksu thrust fault over the last ~16,500 years. Our slip history is based on the three following assumptions.

[33] First, the observed uplift and deformation is earthquake related, and any aseismic slip is negligible. The terrace record testifies the Aksu thrust fault is indeed not continuously creeping. Furthermore, even if aseismic slip following a major earthquake is possible and has been often documented at depth on many faults, it does not usually reach the surface. In addition, faults showing surface creep are not in coarse-grained material such as moraines and boulder conglomerates.

[34] Second, we suppose that seismic slip does not vary much along fault strike. Indeed all scarp profiles are located within 800 m from one another and key profiles are within 400 m of each other. In addition the Aksu thrust along this fault segment show no structural change. So the mean scarp height variations due to a single earthquake are probably

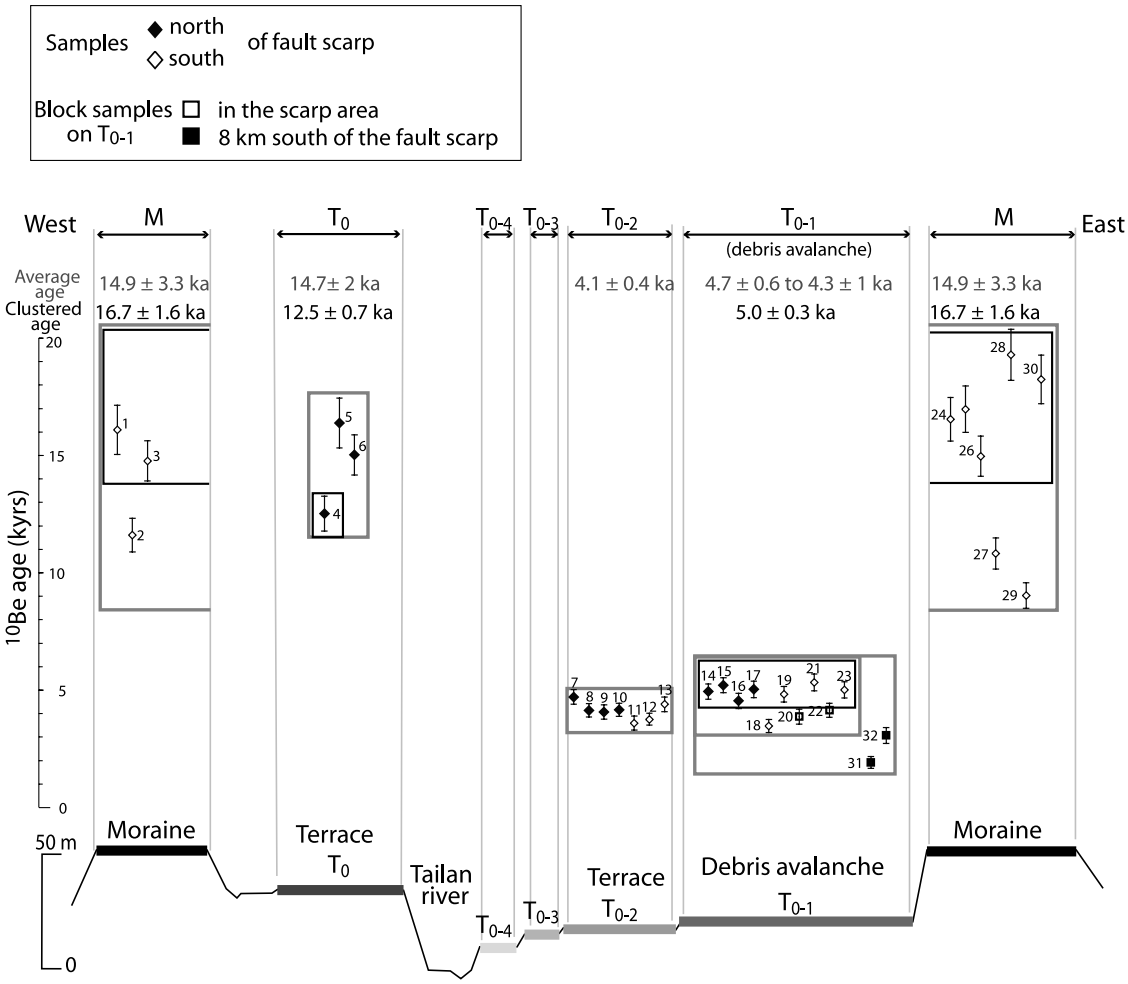

Figure 8. Schematic (bottom) E-W cross section and (top) sample age distribution for the different nested surfaces of the Tailan river valley. Surface ages correlate with their relative height. Clustered averages are calculated by excluding outliers outside rectangles (see text for discussion). Average age for M is from all samples.

negligible, and we infer that we can distinguish surfaces with a cumulated scarp height due to n major earthquakes from one with a scarp due to n + 1 major earthquakes.

[35] Third, we use the uplift measurements at a given point on the Aksu fault to infer the number of major earthquakes on this fault, knowing that earthquakes on a given fault do not always rupture the same fault segments. We argue that the Aksu thrust fault bounding the southern front of the Aksu reentrant extends only over 35 km. In addition, a surface uplift of 1 m in the studied area corresponds to ~2.5 m of fault slip, and earthquake scaling laws imply that the related rupture extends over a length of 50–100 km. So the fault scarp across surfaces in the Tailan River would probably record all the seismic history of this 35-km-long segment since surface abandonment. The eastern extension of the fault into the Kuche fold-and-thrust belt may show a different seismic history.

6.2. Method

[36] To reconstruct the seismic history along the Aksu thrust fault, we do not use the individual scarp height measurements done previously (Figure 6) because they depend on the way we measure these offsets and we do not want to propagate the related potential errors in the inferred deformation history. So we directly compare the scarp profiles across the different surfaces by stacking the profile segments south of the scarp and by fitting fault cuts at the base of the scarp together. The resulting Figure 10 immediately points out the differences in cumulative vertical displacement after each episode of surface abandonment. Our estimates of the vertical difference between surfaces are very well constrained except for the moraine and vary by less than 0.5 m depending on the way we do the fitting. Finally the surface ages are used to constrain the timing of these cumulative earthquake-related surface displacements (Figure 10b).

6.3. Results

[37] Comparison of the scarp profiles across the moraine and T_0 surfaces shows a maximum difference in height of 1.8 m (Figure 10a). The difference in height is variable in profiles and depends on the way we stack the moraine and the T_0 profiles. These variations may be related to the difference in near-surface fault geometry inferred previously. However, the data cannot exclude the possibility that one major earthquake may have occurred

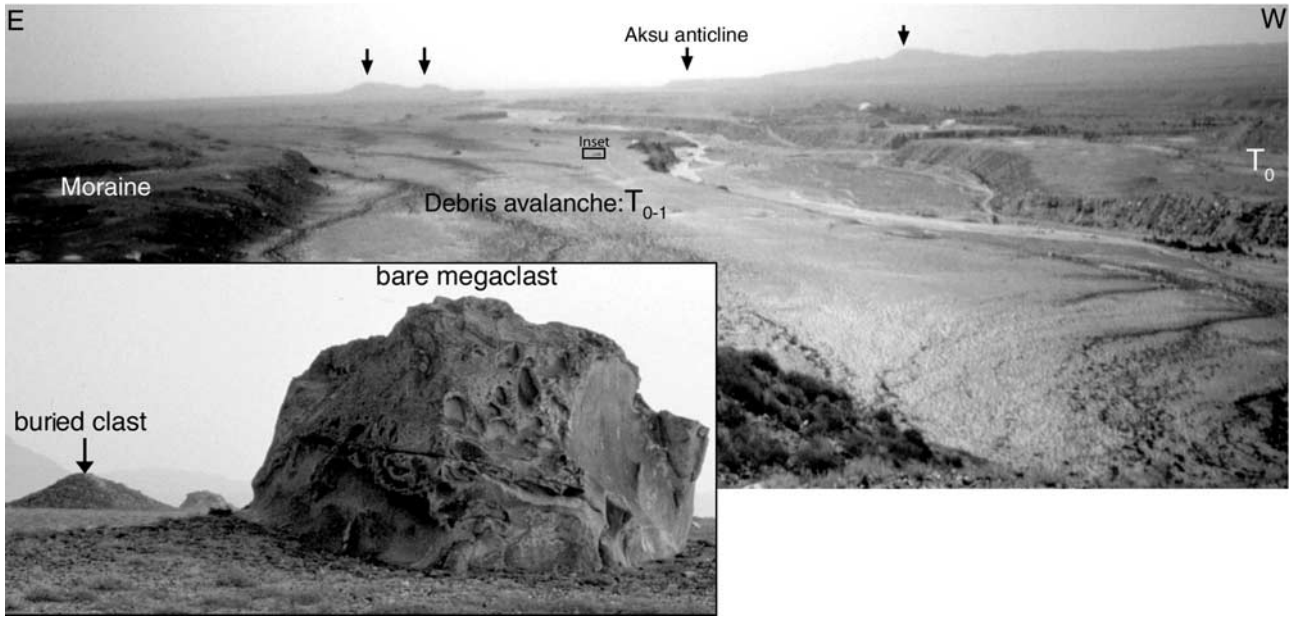

Figure 9. Southward view of the debris avalanche surface $T_{0\text{-}1}$ bounded laterally to the east by moraine M and to the west by terrace T_0. In the distance to the south (see inset) the avalanche surface is scattered with numerous huge blocks, some bare, some covered with debris or mud/soil. A map of large blocks is shown in Figure 2.

after the retreat of the Tailan glacier ~16,500 years ago and before the abandonment of the T_0 terrace ~12,500 years ago.

[38] The T_0 and $T_{0\text{-}1}$ scarp heights and tilts are nearly identical (Figures 6a and 6b) which implies that no major earthquake occurred between the abandonment of T_0 ~12,500 ago and the deposition of $T_{0\text{-}1}$ 5000 years ago. The stacking of profiles in Figure 10a further confirms that the 6 m scarp across both $T_{0\text{-}1}$ and T_0 has formed entirely in the last ~5000 years. Another implication of the similarities in scarp heights is that the debris avalanche was probably not triggered by an earthquake on the Aksu thrust fault, as is sometimes observed for large earthquakes on other faults [e.g., *McSaveney*, 1978; *Van der Woerd et al.*, 2004].

[39] The stacking of profiles across $T_{0\text{-}1}$, $T_{0\text{-}2}$ and $T_{0\text{-}4}$ directly points out the vertical differences between these surfaces across the fault scarp (Figure 10a). For example the $T_{0\text{-}2}$ surface is 1.8 m lower than the $T_{0\text{-}1}$ surface (Figure 10a). In addition, scarps across $T_{0\text{-}2}$ and $T_{0\text{-}3}$ have similar heights and tilt (Figure 6a), and the differential tilt of $T_{0\text{-}2}$ and $T_{0\text{-}3}$ is also smaller (1.7°) than that of T_0 and $T_{0\text{-}1}$ (~2.6°) (Figure 6a). These observations imply that at least one major earthquake occurred after $T_{0\text{-}1}$ and before the abandonment of terrace $T_{0\text{-}2}$ ~4000 years ago, and that no earthquake occurred in the time period between the abandonment of $T_{0\text{-}2}$ and of $T_{0\text{-}3}$. Figure 10a also shows that the $T_{0\text{-}4}$ surface is 0.9 m lower that the $T_{0\text{-}2}$ surface, which implies that an additional earthquake occurred after the abandonment of $T_{0\text{-}3}$, and before the abandonment of $T_{0\text{-}4}$. Finally, the $T_{0\text{-}4}$ surface itself is deformed by a 3.3-m-high scarp, which is the result of one or more subsequent earthquake ruptures.

[40] The comparison of scarp heights between the different surfaces thus allows us to put some constraints on the history of seismic activity on the Aksu fault (Figure 10b). In the last ~5,000 years, the fault repeatedly ruptured in a burst of at least three major earthquakes, whereas during the preceding period the fault was quiet for at least ~7500 years. The seismic cycle along the Aksu thrust fault is thus strongly irregular.

[41] The full nature of the irregularity of the Aksu fault is unknown given the limited number of datable surfaces. For example the data are consistent with a regular seismic cycle with 2 mm/yr of uplift for the last ~5000 years, following a hiatus of ~9000 years. The hiatus could be much longer, spanning ~12,000 years, if we consider that the uplift of the moraine and the T_0 surface are similar and that no major earthquake occurs during this time period. By this scenario the irregularity is a turning on and off of the fault. Alternatively the irregularity might be more fully chaotic.

7. Shortening Rate Across the Aksu Reentrant

7.1. Shortening Rate Across the Aksu Thrust Fault

[42] Because large earthquakes along the Aksu thrust fault occurred with significant irregularity over the last 16,500 years, the ratio between the fault slip and the mean age does not provide a constant slip rate. However, an uplift rate of 2 ± 0.5 mm/yr for the last 5000 years is indicated if we assume a regular seismic cycle for this episode, with a rate of zero for the preceding period (Figure 10b). The meaning of a combined rate is not obvious.

[43] It is not straightforward to translate these uplift rates directly into rates of shortening because of surface folding

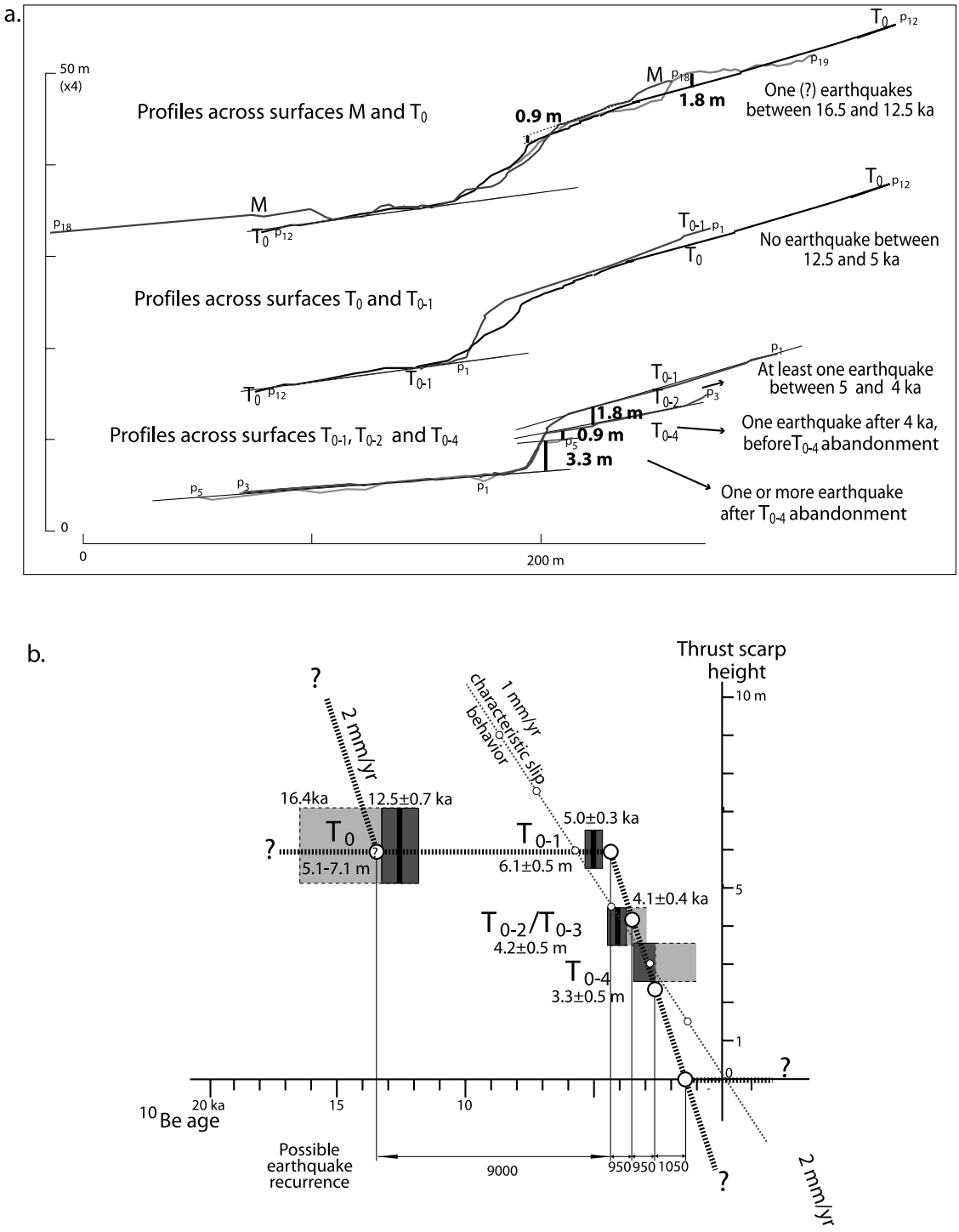

Figure 10. Seismic history for the Aksu thrust fault deduced from surface offset height and age. (a) Summary comparison of scarp height for the different surfaces and deduced seismic history, based on the profiles of Figure 6 and the surface ages of Figure 8. (b) Possible earthquake scenario (thick dashed line) with a burst of earthquakes (big white circles) during short periods of 4 to 5 ka and quiescence of at least 7500 years. Present earthquake scenario agrees with scarp heights, but many others are possible. Also shown is a scenario with a characteristic slip behavior (thin dashed line with small white circles representing characteristic earthquakes), using an average coseismic slip of about 1.5 m and a recurrence time of about 1350 years, which is not in agreement with our surface dating.

in a zone extending ~90–130 m north of the scarp. However, given our progressive near-surface flattening fault model (~4 m of fault slip per meter of scarp height), we get a linear shortening rate of ~8 ± 2 mm/yr for the last ~5000 years across the Aksu thrust fault.

7.2. Shortening Rate Across the Aksu Anticline

[44] To evaluate the total shortening along the southern Tianshan front in Aksu, we must also take into account the deformation accommodated by the Aksu anticline located 12 km south of the Aksu thrust fault (Figure 1b).

[45] This ~100-km-long anticline fold exposes the late Miocene Kanchung Formation in its front limb and core and the Pliocene Kuche Formation in its long back limb. Just east of the Tailan River the fold amplitude decreases sharply and only folded Quaternary alluvial strata outcrop at the surface. These wide southeast sloping alluvial surfaces (labeled T_0 and T_1 in Figure 2) are faulted and folded along the Aksu anticline and can be used to compute a crude shortening rate.

[46] The main alluvial marker is the T_0 fan surface that is continuous across the anticline and thus provides a record of the total shortening across the fold since its deposition (Figure 2). A main ~30-m-high scarp related to the main back thrust deforms the T_0 surface along the northern edge of the anticline. Smaller thrust faults uplift the T_0 surface on the south flank of the anticline by ~1 m and ~5 m, respectively. By adding all the scarp heights we obtain a total fault-related uplift of ~35 m. The amount of folding of the T_0 fan surface was not estimated. So the ~35 m total vertical uplift underestimates the total deformation of the T_0 surface across the Aksu anticline.

[47] The age of the T_0 fan surface can be indirectly constrained by the fact that it is overridden by the debris avalanche. Surface T_0 must be older than 5 ka. Furthermore, T_0 was emplaced during a major fan building episode, which is likely to be related to the return to interglacial conditions after the maximum glacial period marked by the Tailan terminal moraine (~16.5 ka ago). During deglaciation, the temporary increased runoff probably triggered a massive sediment eviction from the high range catchment and the formation of the T_0 fan surface. Similar aggradation of piedmont fans took place at the front of the northern Tianshan ~12,000 years ago [*Poisson and Avouac*, 2004]. The T_0 fan surface may thus have started to form ~12.5 ka ago at the same time as the T_0 terrace emplacement near the mountain front. The building process of this large fan may have taken several thousand years with a probable eastward diachronism. So we can only infer that the fan surface T_0 was emplaced between 5 and 12.5 ka.

[48] Combining the 30-m-high back-thrust scarp, which represent the minimum fault-related uplift of the Aksu anticline, with the inferred maximum age of the surface T_0 yields a minimum uplift rate of 2.4 mm/yr. For a thrust fault ramp with a 30–35° dip estimated from field measurements and seismic lines, the minimum uplift rate inferred would imply a minimum shortening rate of 4.5 ± 0.3 mm/yr across the Aksu anticline over the last 12.5 ka.

7.3. Total Shortening Rate

[49] Given the irregular behavior on the Aksu thrust and a possible switching of activity between the Aksu thrust fault and the frontal Aksu fold, we need to compute the total deformation across both structures by considering average shortening derived from deformed markers of similar ages. As we have computed the minimum shortening across the Aksu fold from the T_0 marker, it is necessary to consider the shortening rate also derived from T_0 for the Aksu thrust fault, which is 2 ± 0.4 mm/yr (20 to 30 m fault slip) over the last 12.5 ka.

[50] Combining our fault slip estimates across the Aksu thrust structure and the Aksu anticline using the T_0 geomorphic marker yields a total shortening rate of at least 6.5 mm/yr along the southern Tianshan front. This estimate agrees with the 8 ± 3 mm/yr shortening inferred from GPS measurements over a 6-year period across the Aksu-Kashi fold-and-thrust belt [*Reigber et al.*, 2001].

8. Discussion

[51] The paleoseismic record along the Aksu thrust fault for the last ~16,500 years is characterized by long quiet period of at least 7500 years with no scarp-forming earthquakes, followed by a clustering of at least three major earthquakes in the last ~5000 years. Similar aperiodic behavior was reported along the Dead Sea Fault zone [*Marco et al.*, 1996]. Other examples of long-term analysis of seismic activity using historical catalogs [*Ambraseys*, 1989; *Vere-Jones and Ozaki*, 1982; *Xu and Deng*, 1996; *Goes*, 1996], paleoseismologic data [*Jacoby et al.*, 1998; *Grant and Sieh*, 1995; *Marco et al.*, 1996; *Wells et al.*, 1999], geomorphological data [*Ritz et al.*, 2003], or geodesic and geologic data [*Friedrich et al.*, 2003] show that periods of activity can alternate with periods of quiescence along a single fault or a group of faults and that many fault zones exhibit temporal earthquake clustering [*Pirazzoli et al.*, 1996]. These observations suggest that a representative record of the long-term behavior of a fault zone may require a knowledge of all strong earthquakes over period exceeding 10,000 years [*Van der Woerd et al.*, 2002].

[52] Aperiodic behavior may have different causes. First, the seismic cycle on a single fault can vary intrinsically. *Becker and Schmeling* [1998] have shown that earthquake recurrence on isolated faults depends on their orientation with respect to the regional stress field. Aperiodicity can simply result from a nonideal orientation of the rupture plane in the simplest possible homogeneous stress field, even when constant loading rate and frictional parameters are assumed. However, the mean N103° strike of the Aksu thrust fault is nearly optimally oriented to accommodate the N12°E shortening direction in Aksu obtained by GPS [*Reigber et al.*, 2001]. Second, the Aksu thrust fault forms the westernmost extension of the Kuche fold-and-thrust belt, and at the extremities of fault systems, particular seismic behavior may be expected for mechanical reasons [*Scholz*, 2002; *Manighetti et al.*, 2001, 2004]. In addition, the westward growth of the Aksu thrust fault is impeded in the Aksu reentrant area by the disappearance of Tertiary and Mesozoic strata. So the Aksu reentrant is probably a mechanical "barrier" showing particular seismic behavior. Third, in regions where multiple faults exist, interaction between faults or even fault segments can determine the seismicity pattern of the system to a great extent. Coulomb modeling [e.g., *Lerner et al.*, 1981; *Li and Kisslinger*, 1985;

King et al., 1994; *Ward and Goes*, 1993; *Harris and Day*, 1993] predicts large event irregularity as a result of a stress transfer. In the Aksu reentrant several structures accommodate the active shortening. Ruptures along the Kalping or Kuche fault systems to the west or east can induce large stress change along the Aksu thrust fault. Furthermore, the Aksu anticline is an active structure located just 12 km south of the Aksu thrust fault, and seismic activity may switch between the two structures. Numerical models of compressive mountain belts suggest that such oscillation can be expected [e.g., *Hardy et al.*, 1998]. Finally, the physical mechanism that has been presumed to underlie the regular recurrence of characteristic earthquakes, which is a steady accumulation of stress due to long-term plate motion, may be wrong, especially in an intracontinental belt. The strain rate presently imaged by GPS data over the Tianshan may vary over a much shorter period of time than previously thought. Whatever the underlying mechanism, strain accumulation and release on the Aksu thrust fault involves complex processes that do not interact in a temporally uniform manner.

9. Conclusions

[53] The uplift of dated geomorphic markers along the Tailan River shows that the Aksu thrust fault, which bounds the high southern Tianshan, is a major active structure that accommodates half of the ~8 mm/yr shortening in this area. These data also constrain the seismic history of the thrust front during the last ~16,500 years. The Aksu thrust fault is characterized by a strongly aperiodic seismic cycle. From ~12.5 to 5 ka the fault was quiet. This ~7500 year period of quiescence was then followed by a seismic cluster of at least three earthquakes in the last ~5000 years. Such complex seismic behavior may be due to intrinsic fault properties at their extremities, or to interaction with adjacent faults. This seismic aperiodicity may also be induced by long-term variations in strain rates across the complex Tianshan range.

Appendix A: Characteristics of the $T_{0\text{-}1}$ Debris Avalanche

[54] A major debris avalanche covers the Tianshan piedmont south of the frontal Aksu thrust fault. In this appendix we describe in some detail the avalanche geometry, surface characteristics and cross-sectional shape.

[55] North of the mountain front, the remnants of the debris avalanche (or $T_{0\text{-}1}$ surface) form a quite narrow nested surface inside the U-shaped Tailan glacial valley. At the mouth of the mountain front, the $T_{0\text{-}1}$ surface expands slightly laterally but remains channeled between the moraine and the main outwash terrace T_0 (Figures 2, 3, and 9). To the south of the terminal moraine the debris avalanche spreads out and then splits into two separated tongues (Figure 2). Each tongue extends over a length of about 10 km. The western tongue is located along the present Tailan river valley extending mostly along its western side. It has been deeply incised by the river. The eastern tongue is better preserved because it covers southeastward sloping surfaces without a major drainage system.

[56] The debris avalanche surface is quite smooth (Figures 9 and A1) suggesting that the avalanche contained water or ice. Large clasts and huge angular megaclasts, generally up to 3–5 m in diameter (Figure 9), some exceeding 10 m, some bare and some covered with soil, are embedded on top of the avalanche surface (Figure 2). The thickness of the avalanche deposit reaches more than 10 m near the mountain front and progressively decreases southward, on the basis of comparison of longitudinal topographic profiles of the eastern flank of the eastern tongue with profiles on nearby alluvial surfaces (Figure A1). The present volume of the debris avalanche mapped south of the Aksu thrust fault may thus reach 0.2 km^3. A similar rock avalanche occurred in 1970 along the Cordillera Blanca in Peru [*Plafker and Ericksen*, 1978; *Vilimek*, 1995]. The two tongues are also characterized by a large-scale transverse topography with ridges on the sides scattered with numerous blocks and with topographic lows almost bare of huge blocks (Figures 2 and A1). This is a characteristic of debris avalanches [*Johnson*, 1984].

[57] The debris avalanche has also a unique structure in outcrop. Figure A2 shows a natural outcrop cross section across the eastern tongue in the area where it covers an alluvial surface along the Tailan River (see location on Figure 2). In the section there is a sharp contrast between the well-rounded and sorted clasts of the alluvium and the unsorted structureless avalanche deposit above. The 1.5 m thick deposit is characterized by debris of all sizes surrounded by a matrix that includes both gravel and a finer fraction (Figure A2). A crude upward coarsening of larger fragments is also visible. The 30 cm basal layer is made of finely crushed rocks or mud. Above this layer, the clasts are not rounded, polished nor striated and have very different lithologies. Apparently the avalanche has mobilized and incorporated vast quantities of morainic material in its path. This is the reason that previous workers were led to interpret this deposit as a moraine [*Zheng*, 1986, 1988; *Zhang and Shao*, 1991], but its morphology and composition clearly identify it as a turbulent rock and mudflow [see also *Hewitt*, 1999]. No clear landslide scar remains visible upstream in the Tailan valley.

Appendix B: Sampling and Cosmogenic Dating

[58] Ages of the terraces, debris avalanche and moraine were obtained by ^{10}Be-^{26}Al surface exposure dating of boulders embedded in the different surfaces [e.g., *Kohl and Nishiizumi*, 1992; *Bierman et al.*, 1995; *Van der Woerd et al.*, 1998, 2002; *Gosse and Phillips*, 2001; *Mériaux et al.*, 2004]. Only the clearest and most well-developed surfaces were selected for exposure dating. Most of the samples were quartz-rich granitic rocks and quartzite. Both small (<20 cm) and large boulders (1–2 m in diameter, and even larger on $T_{0\text{-}1}$, see below) were sampled. Each sample has been located on high-precision images, with elevations checked on 1:100,000 topographic maps, and site conditions described. For all the samples shielding from surrounding mountain slopes is negligible. The sampling area is small enough (<1 km, Figure 3) that the same latitude and longitude has been used for all samples (N 41.613 – E 80.483), except for two samples located about 5 km to

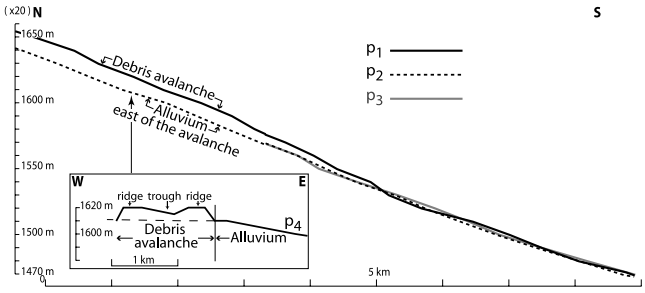

Figure A1. Topographic profiles along and transverse to the eastern lobe of the debris avalanche (see profile locations in Figure 2). Profile p_1 is along the eastern edge of the debris avalanche; profile p_2 is 700 m more to the east on an alluvial surface. Profile p_3 extends from the western edge of the debris avalanche to the overridden alluvial surface. Comparison between profiles implies that debris avalanche thickness, more than 10 m in the north, decreases sharply toward south. Transverse profile p_4 shows the characteristic large-scale topography of debris avalanches with a low in the center and ridges on the sides. The profiles are based on 1:50,000 topographic maps.

the south ($T_{0\text{-}1}$-31_s and $T_{0\text{-}1}$-32_s at N41.553–E80.483; Figure 2).

[59] Clean quartz was separated from the rock samples by using a chemical isolation method [*Kohl and Nishiizumi*, 1992]. The quartz was dissolved in HF and HNO3. Al concentrations were determined both by atomic absorption spectrometry and inductively coupled plasma–mass spectrometry (ICP-MS). A Be carrier and an Al carrier were added as needed. Be and Al were separated by anion and cation exchange ion chromatography in a chloride medium and purified by reprecipitation of the hydroxides. ^{10}Be and ^{26}Al accelerator mass spectrometry (AMS) measurements were carried out at the Lawrence Livermore National Laboratory AMS facility [*Davis et al.*, 1990]. The observed ratios were normalized to ICN ^{10}Be and National Institute of Science and Technology ^{26}Al standards that were diluted by K. Nishiizumi (personal communication, 1995).

[60] Erosion and inheritance were considered negligible, and model ages for ^{10}Be and ^{26}Al were calculated from the expression: $N(t) = P/l\ (1 - \exp(-l/t))$, where N(t) is the nuclide concentration at time t, P is the surface production rate (atom g yr^{-1}) and l is the decay constant of the nuclide (4.591×10^{-7} yr^{-1} for ^{10}Be, 9.832×10^{-7} yr^{-1} for ^{26}Al). Zero-erosion model ages were calculated using a sea level high-latitude (SLHL) ^{10}Be production rate of 5.06 atoms/g quartz/yr. This production rate is based on measurements of glacial surfaces in the Sierra Nevada by *Nishiizumi et al.* [1989] recalculated using the revised 13,000 years glacial retreat ages reported by *Clark et al.* [1995], and rescaled for latitude and altitude using the coefficients of *Lal* [1991], as described by *Owen et al.* [2002]. An uncertainty of 6% on the production rates [*Stone*, 2000] is considered. At the latitude of our site, the variations in the geomagnetic field, as well as the pole position, produce changes in the production rate. These changes can be expressed in terms of an equivalent change in geomagnetic latitude and can be evaluated using the data from *Ohno and Hamano* [1992], *McElhinny and Senanayake* [1982], and the Sint-800 record of *Guyodo and Valet* [1999]. The ages were calculated with the *Stone* [2000] latitude and altitude correction factors using software developed at Lawrence Livermore National Laboratory (D. L. Farber, personal communication, 2002).

[61] Measurements, calculated ages and scaling factors are reported in Table 1. For all samples except two we

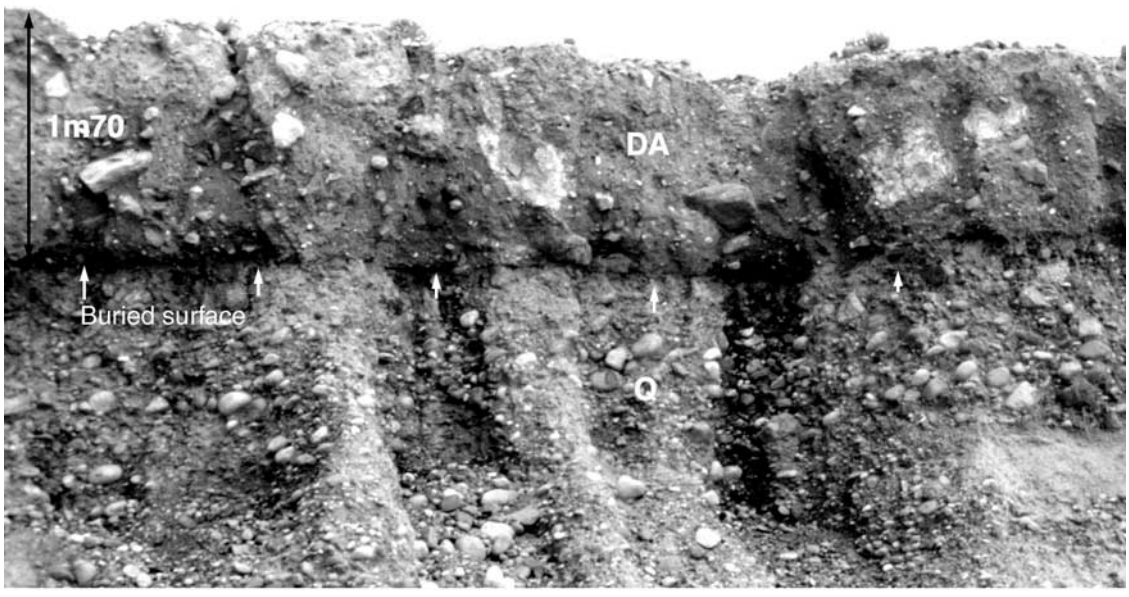

Figure A2. Photograph of a vertical outcrop section through the debris avalanche (DA) and overridden alluvial surface T_0 (see location in Figure 2). The contact between the two surfaces is a finely crushed zone. A chaotic assemblage of fine material, subangular pebbles and boulders, poorly sorted, characterizes the 1.70-m-thick avalanche deposit in that area.

conducted both ^{10}Be and ^{26}Al measurements. While for most of the samples the concentration ratios between Be and Al are consistent, we observe systematically low concentrations for ^{26}Al which are unexplained. We are more confident in the ^{10}Be ages because they rely on a single ratio measurement, whereas the ^{26}Al determinations require two measurements, the ^{26}Al/^{27}Al ratio and the ^{27}Al concentration. For these reasons, we use only the ^{10}Be data in our age calculations, which include the geomagnetic correction. As such, these ages are calibrated and can be directly compared to dates derived from other dating methods (radiocarbon dating, for example).

[62] **Acknowledgments.** This study was supported by NSF EAR-0073759, NSFC 49832040, TPEDB-PetroChina and Princeton 3-D Structure Project. We particularly thank PetroChina for logistic organization in the field and for giving us access to seismic reflection profiles. We also acknowledge strong support from F. J. Ryerson and R. C. Finkel at Lawrence Livermore National Laboratory for cosmogenic dating. Reviews done by James Dolan, Paul Bierman, Jérome Lavé, and Isabelle Manighetti were very helpful in improving the manuscript.

References

Abdrakhmatov, K. Y., et al. (1996), Relative recent construction of the Tian Shan inferred from GPS measurements of the present-day crustal deformation rates, *Nature*, *384*, 450–452.

Allen, M. B., S. J. Vincent, and P. J. Wheeler (1999), Late Cenozoic tectonics of the Kepingtage thrust zone: Interaction between the Tien Shan and the Tarim Basin, northwest China, *Tectonics*, *18*, 639–654.

Ambraseys, N. N. (1989), Temporal seismic quiescence: SE Turkey, *Geophys. J.*, *96*, 311–331.

Avouac, J. P., P. Tapponnier, M. Bai, H. You, and G. Wang (1993), Active thrusting and folding along the northern Tian Shan and late Cenozoic rotation of the Tarim relative to Dzungaria and Kazakhstan, *J. Geophys. Res.*, *98*, 6755–6804.

Bak, P., and C. Tang (1989), Earthquakes as a self-organized critical phenomenon, *J. Geophys. Res.*, *94*, 15,635–15,637.

Becker, T. W., and H. Schmeling (1998), Earthquake recurrence-time variations with and without fault-zone interactions, *Geophys. J. Int.*, *135*, 165–176.

Ben-Zion, Y. (1996), Stress, slip and earthquakes in models of complex single-fault systems incorporating brittle and creep deformations, *J. Geophys. Res.*, *101*, 5677–5706.

Bierman, P. R., A. R. Gillespie, and M. W. Caffee (1995), Cosmogenic ages for earthquake recurrence intervals and debris flow fan deposition, Owens Valley, California, *Science*, *270*, 447–450.

Burbank, D. W., J. K. McLean, M. Bullen, K. Y. Abdrakhmatov, and M. M. Miller (1999), Partitioning of intermontane basins by thrust-related folding, Tien Shan, Kyrgyzstan, *Basin Res.*, *11*, 75–92.

Burchfiel, B. C., E. T. Brown, Q. Deng, X. Feng, J. Li, P. Molnar, J. Shi, Z. Wu, and H. You (1999), Crustal shortening on the margins of the Tien Shan, Xianjiang, China, *Int. Geol. Rev.*, *41*, 665–700.

Carlson, J., and J. Langer (1989), Properties of earthquakes generated by fault dynamics, *Phys. Rev. Lett.*, *62*, 2632–2635.

Chevalier, M. L., P. Tapponnier, R. Ryerson, R. Finkel, J. Van Der Woerd, and Q. Liu (2004), Determination of the slip-rate on the Karakorum fault (Tibet) by dating of radioisotopes (^{10}Be), *Geophys. Res. Abstr.*, *6*, 1607-7962/gra/EGU04-A-05748.

Clark, D. H., P. R. Bierman, and P. Larsen (1995), Improving in-situ cosmogenic chronometers, *Quat. Res.*, *44*, 367–377.

Davis, J. C., I. D. Proctor, J. R. Southon, M. W. Caffee, D. W. Heikkinen, M. L. Roberts, K. W. Turteltaub, D. E. Nelson, D. H. Loyd, and J. S. Vogel (1990), LLNL/UC AMS facility and research program: Nuclear instruments and methods, *Phys. Res.*, *B52*, 269–272.

Friedrich, A. M., B. P. Wernicke, N. A. Niemi, R. A. Bennett, and J. L. Davis (2003), Comparison of geodetic and geologic data from the Wasatch region, Utah, and implications for the spectral character of Earth deformation at periods of 10 to 10 million years, *J. Geophys. Res.*, *108*(B4), 2199, doi:10.1029/2001JB000682.

Gasse, F., M. Arnold, J. C. Fontes, M. Fort, E. Gibert, A. Huc, B. Li, Y. Li, Q. Liu, F. Melieres, C. E. Van, F. Wang, and Q. Zhang (1991), A 13,000-year climate record from western Tibet, *Nature*, *353*(6346), 742–745.

Gibbs, A. D. (1983), Balanced cross-section construction from seismic sections in areas of extensional tectonics, *J. Struct. Geol.*, *5*, 153–160.

Goes, S. D. B. (1996), Irregular recurrence of large earthquakes; an analysis of historic and paleoseismic catalogs, *J. Geophys. Res.*, *101*, 5739–5749.

Gosse, J., and F. M. Phillips (2001), Terrestrial in situ cosmogenic nuclides: Theory and application, *Quat. Sci. Rev.*, *20*, 1475–1560.

Grant, L. B., and K. Sieh (1995), Paleoseismic evidence of clustered earthquakes on the San Andreas Fault in the Carrizo Plain, California, *J. Geophys. Res.*, *99*, 6819–6841.

Guyodo, Y., and J. P. Valet (1999), Global changes in intensity of the Earth's magnetic field during the past 800 kyr, *Nature*, *399*, 249–252.

Hardy, S., C. Duncan, J. Masek, and D. Brown (1998), Minimum work, fault activity and the growth of critical wedges in fold and thrust belts, *Basin Res.*, *10*, 365–373.

Harris, R. A., and S. M. Day (1993), Dynamics of fault interaction; parallel strike-slip faults, *J. Geophys. Res.*, *98*, 4461–4472.

Hewitt, K. (1999), Quaternary moraines vs catastrophic rock avalanches in the Karakoram Himalaya, northern Pakistan, *Quat. Res.*, *51*, 220–237.

Jacoby, G. C., P. R. Sheppard, and K. E. Sieh (1998), Irregular recurrence of large earthquakes along the San Andreas Fault; evidence from trees, *Science*, *241*, 196–199.

Johnson, A. M. (1984), Debris flow, in *Slope Instability,* edited by D. Brunsden and D. B. Prior, pp. 257–361, John Wiley, Hoboken, N. J.

King, G. C. P., R. S. Stein, and J. Lin (1994), Static stress changes and the triggering of earthquakes, *Bull. Seismol. Soc. Am.*, *84*, 935–953.

Kohl, C. P., and K. Nishiizumi (1992), Chemical isolation of quartz for measurement of in-situ produced cosmogenic nuclides, *Geochim. Cosmochim. Acta*, *56*, 3583–3587.

Lal, D. (1991), Cosmic ray labeling of erosion surfaces: In situ production rates and erosion models, *Earth Planet. Sci. Lett.*, *104*, 424–439.

Lasserre, C., et al. (1999), Postglacial left slip-rate and past occurrence of *M*8 earthquakes on the western Haiyuan fault, Gansu, China, *J. Geophys. Res.*, *104*, 17,633–17,651.

Lasserre, C., Y. Gaudemer, P. Tapponnier, A.-S. Mériaux, J. Van der Woerd, Y. Daoyang, F. J. Ryerson, R. C. Finkel, and M. W. Caffee (2002), Fast late Pleistocene slip rate on the Leng Long Ling segment of the Haiyuan fault, Qinghai, China, *J. Geophys. Res.*, *107*(B11), 2276, doi:10.1029/2000JB000060.

Lerner, F. K., V. C. Li, and J. R. Rice (1981), Stress diffusion along rupturing plate boundaries, *J. Geophys. Res.*, *86*, 6155–6169.

Li, V. C., and C. Kisslinger (1985), Stress transfer and nonlinear stress accumulation at subduction-type plate boundaries: Application to the Aleutians, *Pure Appl. Geophys.*, *122*, 813–829.

Manighetti, I., G. C. P. King, Y. Gaudemer, C. Scholz, and C. Doubre (2001), Slip accumulation and lateral propagation of active normal faults in Afar, *J. Geophys. Res.*, *106*, 13,667–13,696.

Manighetti, I., G. C. P. King, and C. Sammis (2004), The role of off-fault damage in the evolution of normal faults, *Earth Planet. Sci. Lett.*, *217*, 399–408.

Marco, S., M. Stein, A. Agnon, and H. Ron (1996), Long-term earthquake clustering; a 50,000-year paleoseismic record in the Dead Sea graben, *J. Geophys. Res.*, *101*, 6179–6191.

McElhinny, M. W., and W. E. Senanayake (1982), Variations in the geomagnetic dipole: 1. The past 50,000 years, *J. Geomagn. Geoelectry.*, *34*, 39–51.

McSaveney, M. J. (1978), Sherman Glacier rock avalanche, Alaska, USA, in *Rockslides and Avalanches*, edited by B. Voight, pp. 197–258, Elsevier, New York.

Mériaux, A.-S., F. J. Ryerson, P. Tapponnier, J. Van der Woerd, R. C. Finkel, X. Xu, Z. Xu, and M. W. Caffee (2004), Rapid slip along the central Altyn Tagh Fault: Morphochronologic evidence from Cherchen He and Sulamu Tagh, *J. Geophys. Res.*, *109*, B06401, doi:10.1029/2003JB002558.

Molnar, P., and P. Tapponnier (1975), Cenozoic tectonics of Asia: Effects on a continental collision, *Science*, *189*, 419–426.

Nishiizumi, K., E. L. Winterer, C. P. Kohl, J. Klein, R. Middleton, D. Lal, and J. R. Arnold (1989), Cosmic ray production rates of ^{10}Be and ^{26}Al in quartz from glacially polished rocks, *J. Geophys. Res.*, *94*, 17,907–17,915.

Ohno, M., and Y. Hamano (1992), Geomagnetic poles over the past 10,000 years, *Geophys. Res. Lett.*, *19*, 1715–1718.

Owen, L. A., M. Caffee, R. Finkel, L. Gualtieri, J. Q. Spencer, and B. Richards (1999), Timing of late Quaternary glaciations throughout the Himalayas, *Geol. Soc. Am. Abstr. Programs*, *31*, 141.

Owen, L. A., R. C. Finkel, M. W. Caffee, and L. Gualtieri (2002), Timing of multiple late Quaternary glaciations in the Hunza Valley, Karakoram Mountains, northern Pakistan: Defined by cosmogenic radionuclide dating of moraines, *Geol. Soc. Am. Bull.*, *114*, 593–604.

Owen, L. A., J. Q. Spencer, H. Ma, P. L. Barnard, E. Derbyshire, R. C. Finkel, M. W. Caffee, and Y. N. Zeng (2003), Timing of Late Quaternary glaciation along the southwestern slipes of the Qilian Shan, Tibet, *Boreas*, *32*, 281–291, doi:10.1080/03009480310001632.

Pirazzoli, P. A., J. Laborel, and S. C. Stiros (1996), Earthquake clustering in the eastern Mediterranean during historical times, *J. Geophys. Res.*, *101*, 6083–6097.

Plafker, G., and G. E. Ericksen (1978), Nevados Huascaran avalanches, Peru, in *Rockslides and Avalanches*, edited by B. Voight, pp. 277–314, Elsevier, New York.

Poisson, B., and J. P. Avouac (2004), Holocene hydrological changes inferred from alluvial stream entrenchment in North Tian Shan (northwestern China), *J. Geol.*, *112*, 231–249.

Reigber, C., G. W. Michel, R. Galas, D. Angermann, J. Klotz, J. Y. Chen, A. Papschev, R. Arslanov, V. E. Tzurkov, and M. C. Ishanov (2001), New space geodetic constraints on the distribution of deformation in central Asia, *Earth Planet. Sci. Lett.*, *191*, 157–165.

Rhodes, T. E., F. Gasse, L. Ruifen, J. C. Fontes, K. Wei, P. Bertrand, E. Gibert, F. Mélières, P. Tucholka, Z. Wang, and Z. Y. Cheng (1996), A late Pleistocene-Holocene lacustrine record from Lake Manas, Zunggar (northern Xinjiang, western China), *Palaeogeogr. Palaeoclimatol. Palaeoecol.*, *120*, 105–121.

Richards, B. W., L. A. Owen, and E. J. Rhodes (2000), Timing of late Quaternary glaciations in the Himalayas of northern Pakistan, *J. Quat. Sci.*, *15*, 283–297.

Ritz, J.-F., et al. (2003), Late Pleistocene to Holocene slip rates for the Gurvan Bulag thrust fault (Gobi-Altay, Mongolia) estimated with ^{10}Be dates, *J. Geophys. Res.*, *108*(B3), 2162, doi:10.1029/2001JB000553.

Schäfer, J. M., S. Tschudi, Z. Zhao, X. Wu, S. Ivy-Ochs, R. Wieler, H. Baur, P. W. Kubik, and C. Schlüchter (2002), The limited influence of glaciations in Tibet on global climate over the past 170,000 yr, *Earth Planet. Sc. Lett.*, *194*, 287–297.

Scholz, C. (2002), *The Mechanics of Earthquakes and Faulting*, 2nd ed., Cambridge Univ. Press, New York.

Shaw, B., and J. Rice (2000), Existence of continuum complexitiy in the elastodynamics of repeated faulty ruptures, *J. Geophys. Res.*, *105*, 791–823.

Stone, J. O. (2000), Air pressure and cosmogenic isotope production, *J. Geophys. Res.*, *105*, 23,753–23,759.

Suppe, J., C. D. Connors, and Y. K. Zhang (2004), Shear fault-bend folding, in *Thrust Tectonics*, edited by K. R. McClay, *AAPG Mem.*, *82*, 303–323.

Tapponnier, P., and P. Molnar (1979), Active faulting and Cenozoic tectonics of the Tien Shan, Mongolia and Baykal regions, *J. Geophys. Res.*, *84*, 3425–3459.

Thompson, L. G., et al. (1997), Tropical climate instability: The last glacial cycle from a Qinghai-Tibetan ice core, *Science*, *276*, 1821–1825.

Thompson, S. C., R. J. Weldon, C. M. Rubin, K. Abdrakhmatov, P. Molnar, and G. W. Berger (2002), Late Quaternary slip rates across the central Tien Shan, Kyrgyzstan, central Asia, *J. Geophys. Res.*, *107*(B9), 2203, doi:10.1029/2001JB000596.

Van der Woerd, J., F. J. Ryerson, P. Tapponnier, Y. Gaudemer, R. Finkel, A. S. Mériaux, M. Caffee, G. Zhao, and Q. He (1998), Holocene left-slip rate determined by cosmogenic surface dating on the Xidatan segment of the Kunlun fault (Qinghai, China), *Geology*, *26*, 695–698.

Van Der Woerd, J., X. Xu, H. Li, P. Tapponnier, B. Meyer, F. J. Ryerson, A. S. Mériaux, and Z. Xu (2001), Rapid active thrusting along the northwestern rangefront of the Tanghenan Shan (western Gansu, China), *J. Geophys. Res.*, *106*, 30,475–30,504.

Van der Woerd, J., et al. (2002), Uniform post-glacial slip-rate along the central 600 km of the Kunlun fault (Tibet), from ^{26}Al, ^{10}Be and ^{14}C dating of river offsets, and climatic origin of the regional morphology, *Geophys. J. Int.*, *148*, 356–388.

Van der Woerd, J., L. A. Owen, P. Tapponnier, X. Xu, F. Kervyn, R. C. Finkel, and P. L. Barnard (2004), Giant *M*8 earthquake-triggered ice avalanches in the eastern Kunlun Shan, northern Tibet: Characteristics, nature and dynamics, *Geol. Soc. Am. Bull.*, *116*, 394–406.

Vere-Jones, J. D., and T. Ozaki (1982), Some examples of statistical estimation applied to earthquake data, *Ann. Inst. Stat. Math.*, *34*, 189–207.

Vilimek, V. (1995), Natural hazards in the Cordillera Blanca Mts., Peru, *Acta Mont., Ser. A Geodyn.*, *8*, 71–86.

Ward, S. N., and S. D. B. Goes (1993), How regularly do earthquakes recur? A synthetic seismicity model for the San Andreas fault, *Geophys. Res. Lett.*, *20*, 2131–2134.

Wells, A., M. D. Yetton, R. P. Duncan, and G. H. Stewart (1999), Prehistoric dates of the most recent Alpine fault earthquakes, New Zealand, *Geology*, *27*, 995–998.

White, N. J., J. A. Jackson, and D. P. McKenzie (1986), The relationship between the geometry of normal faults and that of the sedimentary layers in their hanging walls, *J. Struct. Geol.*, *8*, 897–909.

Xiao, H. B., and J. Suppe (1989), Role of compaction in listric shape of growth normal faults, *AAPG Bull.*, *73*, 777–786.

Xu, X., and Q. Deng (1996), Nonlinear characteristics of paleoseismicity in China, *J. Geophys. Res.*, *101*, 6209–6231.

Yin, A., S. Nie, P. Craig, T. M. Harrisson, F. J. Ryerson, X. Qian, and G. Yang (1998), Late Cenozoic tectonic evolution of the southern Chinese Tian Shan, *Tectonics*, *17*, 1–27.

Zhang, Z., and S. Shao (Eds.) (1991), *The Quaternary of China, 13th INQUA Congress*, 575 pp., China Ocean Press, Beijing.

Zheng, B. (1986), Glacial geomorphological map (1:200,000) of Mt. Tomur Region, Tian Shan, *Ann. Glaciol.*, *8*, 209.

Zheng, B. (1988), Studies of the glacial characteristics and environment of the last glaciation in west China, in *The Paleoenvironment of East Asia From the Mid-Tertiary*, *Proceeding of the Second Conference*, edited by P. Whyte et al., pp. 453–463, Cet. of Asian Stud. Univ. of Hong Kong, Hong Kong.

A. Hubert-Ferrari, Institut de Géologie, Université de Neuchatel, rue Emile Argand 11, Neuchâtel, CH-2007, Switzerland. (aurelia.ferrari@unine.ch)

H. Lu, Department of Earth Sciences, Nanjing University, Nanjing 210093, China.

J. Suppe, Department of Geosciences, Princeton University, Princeton, NJ 08544, USA.

J. Van Der Woerd, IPGS, CNRS UMR 7516, 5, rue Rene Descartes, F-67084 Strasbourg Cedex, France.

X. Wang, Geosciences Department, Zhejiang University, Hangzhou 310027, China.